Naturaliste Plateau: Constraints on the Timing and Evolution of the Kerguelen Large Igneous Province and its Role in Gondwana Breakup

Nicholas G. Direen[a, b]*, Benjamin E. Cohen[c, d], Roland Maas[e], Frederick A. Frey[f], Joanne M. Whittaker[b], Millard F. Coffin[b, g], Sebastien Meffre[a, h], Jacqueline A. Halpin[a, b, h] and Anthony J. Crawford[a, h].

[a] School of Physical Sciences, University of Tasmania, Private Bag 126, Hobart TAS 7001, Australia

[b] Institute for Marine and Antarctic Studies, University of Tasmania, Private Bag 129, Hobart TAS 7001, Australia

[c] School of Earth Sciences, The University of Queensland, St Lucia QLD 4072, Australia

[d] Scottish Universities Environmental Research Centre, East Kilbride, G75 0QF, UK

[e] School of Earth Sciences, University of Melbourne, Parkville, VIC 3010, Australia

[f] Earth, Atmosphere and Planetary Sciences, Massachusetts Institute of Technology, Cambridge, MA 02139-4307, USA

[g] Woods Hole Oceanographic Institution, Woods Hole, MA 02543-1050, USA

[h] ARC Centre of Excellence in Ore Deposits and School of Physical Sciences, University of Tasmania, Private Bag 126, Hobart TAS 7001, Australia

*Corresponding author: email n_direen@utas.edu.au; cell +1 727-517-6874

Postal address: 2523 Bridgestone Park Ln, Spring TX 77386 USA

Abstract

Volcanism associated with the Kerguelen Large Igneous Province is found scattered in southwestern Australia (the ~136 to ~130 Ma Bunbury Basalts, and ~124 Ma Wallaby Plateau), India (~118 Ma Rajmahal Traps and Cona Basalts), and Tibet (the ~132 Ma Comei Basalts), but apart from the ~70,000 km^2 Wallaby Plateau, these examples are spatially and volumetrically minor. Here, we report dredge, geochronological, and geochemical results from the ~90,000 km^2 Naturaliste Plateau, located ~170 to ~500 km southwest of Australia. Dredged lavas and intrusive rocks range from mafic to felsic compositions, and prior geophysical analyses indicate these units comprise much of the plateau substrate. $^{40}Ar/^{39}Ar$ plagioclase ages from mafic units and U-Pb zircon ages from silicic rocks indicate magmatic emplacement from 130.6 ± 1.2 to 129.4 ± 1.3 Ma for mafic rocks, and 131.8 ± 3.9 to 128.2 ± 2.3 Ma for silicic rocks (2σ). These Cretaceous Naturaliste magmas incorporated a significant component of continental crust, with relatively high $^{87}Sr/^{86}Sr$ (up to 0.78), high $^{207}Pb/^{204}$ Pb ratios (15.5-15.6), low $^{143}Nd/^{144}Nd$ (0.511-0.512), and primitive-mantle normalized (Th/Nb of 11.3 and La/Nb of 3.97. These geochemical results are consistent with the plateau being underlain by continental basement, as indicated by prior interpretations of seismic and gravity data, corroborated by dredging of Mesoproterozoic granites and gneisses on the southern plateau flank. The Cretaceous Naturaliste Plateau igneous rocks have signatures indicative of extraction from a depleted mantle, with trace element and isotopic values that overlap with Kerguelen Plateau lavas indicative of crustal contamination. Our chemical and geochronological results therefore indicate the Naturaliste Plateau contains evidence of an extensive igneous event representing some of the earliest voluminous Kerguelen hotspot magmas. Prior work indicates that contemporaneous correlative volcanic sequences

underlie the nearby Mentelle Basin, and the Enderby Basin and Princess Elizabeth Trough in the Antarctic. When combined, the igneous rocks in the Naturaliste, Mentelle, Wallaby, Enderby, Princess Elizabeth, Bunbury, and Comei-Cona areas form a 136-124 Ma Large Igneous Province covering >244,000 km^2.

Keywords: Naturaliste Plateau; Kerguelen hotspot; Gondwanaland breakup; geochronology; geochemistry; Tibet, Wallaby Plateau.

1. Introduction

The comparatively well-studied, largely submarine Kerguelen Large Igneous Province (LIP) and its conjugate rifted fragment, Broken Ridge (Mutter and Cande, 1983; Tikku and Cande, 2000), together with its onshore correlatives in southwestern Australia (Frey et al., 1996; Olierook et al., 2016), northeastern India (Coffin et al., 2002; Kent et al., 2002; Kent et al., 1997), and Tibet (Zhu et al., 2008; Zhu et al., 2009), form the second largest known LIP preserved on Earth (Fig. 1a). Geochronologic dating of these LIP fragments, now widely separated by rifting, show varying clusters – an apparently spatially minor early component around 137-130 Ma, exposed onshore in Western Australia (the Bunbury Basalt: Fig. 1b; Frey et al., 1996, Olierook et al., 2016); and a volumetrically major cluster, which commenced later, around at 124-118 Ma in the main Kerguelen Plateau (Coffin et al., 2002), and the Wallaby Plateau (Olierook et al., 2015) as well as the smaller volumes in south Asia (Coffin et al., 2002; Zhu et al., 2008, 2009).

The age discrepancy between onset of hotspot volcanism around ~137 Ma, and major expression of volcanism some 13-19 Ma later, have led to speculation about the possibility of a Kerguelen mantle plume "incubating" beneath the extending Gondwana lithosphere (Coffin et al., 2002; Kent et al., 2002; Kent et al., 1992; Zhu et al., 2008). Furthermore, despite the large size of the Kerguelen LIP, it is not currently considered to have played a driving role in breakup of the Gondwana supercontinent, as the voluminous 120-118 Ma Kerguelen eruptions post-date rifting by 10-14 Ma (Coffin and Eldholm, 1992).

There are, however, other rifted fragments of the Kerguelen LIP present in the Indian Ocean basin (Fig. 1, 2), which must be evaluated to fully assess links between

the LIP and rifting, and to evaluate the models invoking "plume incubation". In particular, the ca. 90,000 km^2 Naturaliste Plateau, offshore from Western Australia, (Fig. 1b) has been previously correlated with the Kerguelen LIP based on examination of sparse reconnaissance material (Storey et al., 1992; Coffin and Eldholm, 1992; Mahoney et al., 1995).

In this study, we report the results of further extensive dredging of the Naturaliste Plateau by the R/V *Southern Surveyor* in 2005, in order to investigate the origin of this oceanic feature. We present new geochemical and geochronological data from mafic and felsic igneous rocks dredged from the southern margin of the plateau. We then outline how these new data, together with seismic observations from the Naturaliste Plateau and adjacent Mentelle Basin, indicate the formation of a LIP by Kerguelen hotspot impact into the evolving Australia-Antarctica + India-Madagascar spreading margin.

2. Regional Setting

The Naturaliste Plateau is a quasi-rectangular ~250 by 400 km submarine massif rising ~2500 m above the surrounding seafloor to water depths of ~1600 m (Fig. 1b). It covers ~90,000 km^2 and is separated by a deep, ~170 km wide trough from the southwest Australian mainland (Fig. 1b). The Naturaliste Plateau is related to the adjacent more deeply subsided Mentelle Basin (Fig 1b; Maloney et al., 2011), which occupies a further ~44,000 km^2. The Naturaliste Plateau and Mentelle Basins are located at the intersection of two rift arms formed during Gondwana breakup (Petkovic, 1975; Jongsma and Petkovic, 1977; Powell et al., 1988; Royer and Coffin, 1992; Direen et al., 2007; Direen et al., 2008) (Fig. 2). Rifting between India-Madagascar and Australia-Antarctica commenced in the Callovian (~165 Ma) in the

Argo Abyssal Plain (Fig. 1a), and rapidly propagated southwards during the Valanginian–Hauterivian (Fig. 2; 140 Ma – 130 Ma: Markl, 1978; Veevers and Li, 1991; Mihut and Mueller, 1998; Gaina et al., 2007), producing a rifted margin on the Australia-Antarctic plate, conjugate to Greater India. North of the Wallaby-Zenith Fracture Zone (Fig. 1a), the rifted margin is voluminously magmatic, with extensive seaward-dipping reflector sequences (Planke et al., 2000; Direen et al., 2008), and high velocity lower crust, extending south into the Houtman Sub-basin (Fig 1a). In contrast, in the Zeewyck and Vlaming sub-basins of the Perth Basin (Fig. 1a), no seaward-dipping reflector sequences or high velocity lower crust have been documented, and the margin is considered weakly magmatic (Bradshaw et al., 2003), with the presence of discrete volcanic centres (Gorter and Deighton, 2002; Dadd et al. 2015), which are also imaged seismically in the Mentelle Basin (Maloney et al., 2011). The volcanic margin north of the Wallaby-Zenith Fracture Zone predates the earliest currently known 124 Ma (Aptian) onset of Kerguelen Plateau-related hotspot volcanism (Olierook et al., 2015; Duncan, 2002).

The southern Australian continental margin east of the Naturaliste Plateau is not well studied (Bradshaw et al., 2003), but contains onshore volcanic and intrusive rocks of the Bunbury Basalt (Coffin and Eldholm, 1992; Frey et al., 1996; Duncan, 2002; Ingle et al., 2004; Olierook et al., 2016). The Bunbury Basalt contains two geochemical suites: the Casuarina and Gosselin Suites (Frey et al., 1996), and three distinct phases of eruption, at 136.96 ± 0.43 Ma, 132.71 ± 0.43 Ma and 130.45 ± 0.82 Ma (Olierook et al., 2016). The Bunbury Basalt has been correlated with the Rajmahal Traps (Fig. 1a) of eastern India (Coffin and Eldholm, 1992; Frey et al., 1996; Kent et al., 1997), which are dated at 118.1 ± 0.3 Ma (Kent et al., 2002). The Bunbury Basalt and Rajmahal Traps have been linked to the Kerguelen mantle

hotspot (Coffin and Eldholm, 1992; Frey et al., 1996; Kent et al., 1997, Duncan, 2002; Ingle et al., 2004; Olierook et al., 2016).

The southern margin of the Naturaliste Plateau, between Australia and Antarctica, began rifting in Jurassic time (Callovian: ~165 Ma; Totterdell et al., 2000; Direen et al., 2007; Tikku and Direen, 2008; Maloney et al., 2011; Direen, 2011). At ~95 Ma (Cenomanian) mafic volcanism occurred on the co-joined Broken Ridge and Kerguelen Plateau (Fig.1a, 2) (Mutter and Cande, 1982; Tikku and Cande, 2000; Duncan, 2002). Highly diachronous breakup between Australia and Antarctica and propagation of the Southeast Indian Ridge to the southeast in the late Cretaceous (Tikku and Direen, 2008; Direen et al., 2013) formed a magma-poor, hyperextended margin (Sayers et al., 2001; Direen et al., 2007, 2011, 2013). Break-up south of the Naturaliste Plateau appears to have taken place between ~90 and ~84 Ma (Fig.2, Turonian-Santonian) (Beslier et al., 2004). Extreme thinning outpaced magma supply (e.g. Peron-Pinvidic and Manatschal, 2009), resulting in exhumation and marine flooding of the lower crust (Halpin et al., 2008) and mantle (Beslier et al., 2004) at the southern margin of the Naturaliste Plateau, and in the Diamantina Zone (Fig. 1b), respectively.

3. Existing geological knowledge and sampling of the Naturaliste Plateau

Based on seismic and gravity data, the middle crust of the Naturaliste Plateau is incised by probable Palaeozoic and Mesozoic rift basins (Borissova, 2002; Direen et al., 2007). The upper crust of the plateau comprises volcanic rocks and >2 km of post-Turonian sediments (Burkle et al., 1967; Ford, 1975; Borissova, 2002; Maloney et al., 2011).

The first basement samples from the Naturaliste Plateau were obtained by the USNS *Eltanin* in 1972, from a single site on the northeastern plateau (Fig. 1b). This dredge recovered manganese crusts containing 0.5-15 cm conglomerate cobbles set in a matrix of manganese oxide and detrital grains of quartz, plagioclase, clinopyroxene, and garnet-bearing protoliths (Heezen and Tharp, 1973; Coleman et al., 1982). The cobbles were initially interpreted as continental fragments (Heezen and Tharp, 1973), but major and trace element analyses showed them to be mafic aphyric or plagioclase-phyric tholeiitic basalts (Coleman et al., 1982; Mahoney et al., 1995; Storey et al., 1992). The presence of cobbles indicates erosion and transport in a high-energy environment, of at least at or above wave base, implying the site of eruption of the lavas on the Naturaliste Plateau was not always as deeply submerged as it is today.

Further sampling of the Naturaliste Plateau was undertaken by the Deep Sea Drilling Project (DSDP). Two holes (Sites 258 and 264, Fig. 1b) terminated in pre-Cenomanian and middle–late Albian sedimentary sequences (Davies et al., 1974; Ford, 1975; Hayes et al., 1975). Importantly, the lowermost 35 meters at Site 264 recovered conglomerate containing abundant mafic clasts (Ford, 1975; Hayes et al., 1975). This shows that both the northeastern (Site 258) and southern (Site 264) plateau contain mafic lavas, which could have been erupted at or above wave base.

In 1998, dredging from N/O *Marion Dufresne* recovered basalt lavas, dolerite, gabbro, and diorite, along with a small number of granite and gneiss fragments (Beslier et al., 2004).

4. Sampling of the Naturaliste Plateau by the R/V *Southern Surveyor*

In 2005 the R/V *Southern Surveyor* dredged the steep margins of the plateau, with the best samples obtained from the southern flanks (Crawford, 2005; Fig. 1b). Of 28

attempted bottom haul chain dredges, 11 yielded useable igneous rocks (Table 1, Fig. 1b), 11 dredges were empty, and the remainder contained only sediments (Crawford 2005). The igneous samples were dominantly mafic with varying degrees of seafloor alteration (Tables 1 and 2, Supplementary Material Appendix 1). Some dredges recovered a mixture of rock types, including basalt lavas, dolerites, rhyolite, and granodiorite (Supplementary Material Appendix 1), and were probably sampled from talus slopes comprising material from several lithostratigraphic units. Seafloor alteration was variable, ranging from minor to extreme, and usually takes the form of smectite replacing glass, and clay replacing plagioclase. The least altered samples from several dredges were selected for detailed petrographic and geochemical analysis.

The dredged basalt lavas are aphyric or plagioclase+augite-phyric and represent a variety of submarine eruption styles, including: massive lava, pillow lava lacking vesicles, lava breccia, hyaloclastite, and highly vesicular lava (Supplementary Material Appendix 1). The sample suite does not contain material from unambiguously subaerial eruptions.

In addition to the lavas, some dredges recovered medium-grained rocks (e.g., dolerite, granophyre) presumably from intrusive units. Dolerite samples (DR7-2, 7-5, 10-39, 11-19, 11-25, 12-20, 13-7, 21-17) are uniformly medium-grained rocks composed of augite, plagioclase and Fe-Ti oxides. Felsic granophyre in DR10-16 (dredged with gabbro, DR10-14, dolerite DR10-39, and basalts DR10-7 10-67, 10-164) may derive from the last-crystallized part of a thick gabbroic or doleritic sill. Several blocks of formerly glassy, often spherulitic quartz+K-feldspar-phyric rhyolite (DR7-12, DR12-41) were recovered among the basalts and dolerites.

In addition to these mafic and felsic igneous rocks, two *Southern Surveyor* dredges (DR18 and DR21, Fig. 1) also contained fragments of continental crustal rocks, comprising felsic gneiss, microcline phyric granite, felsic orthogneiss and hornblende-garnet gneissic diorite (Halpin et al., 2008). Inside of some thin metamorphic rims of Cambrian age (Halpin et al., 2008, and see below), zircon cores in these rocks yielded U-Pb crystallization ages of 1177 ± 28 Ma (DR18-4, gneiss, n = 10) and 1154 ± 25 Ma (DR21-1, gneiss, n = 15). Chemical (total U-Th-Pb) ages for monazites in two gneisses are much younger (515 ± 5 Ma DR18-4, n = 23 analyses of 10 crystals; 515 ± 7 Ma DR21–3, n = 49 analyses of 23 crystals), and together with the zircon metamorphic rims, suggest that peak thermal metamorphism in these rocks was related to the Cambrian Pinjarra Orogeny of southwest Western Australia (Halpin et al., 2008). The presence of these old mid-crustal continental rocks at two *Southern Surveyor* and one *Marion Dufrense* dredge sites, along with the more widespread occurrence of mafic+felsic igneous activity, is consistent with seismic and gravity data that indicate that the plateau is underlain by thinned (12.5-16 km) continental crust capped by volcanic rocks (Direen et al. 2007), unlike initial suggestions which envisaged the plateau to be constructed entirely from juvenile oceanic erupted material (Coleman et al., 1982; Coffin and Eldholm, 1992).

5. Geochronology

The age and duration of igneous activity on the southern Naturaliste Plateau was examined using $^{40}Ar/^{39}Ar$ dating of plagioclase from a basalt and two dolerites and U-Pb dating of zircon from a granophyre, a monzodiorite and a rhyolite, all selected from the R/V *Southern Surveyor* dredge sample suites.

5.1 Laser ablation ICP-MS zircon U-Pb dating

LA-ICP-MS dating of zircons was carried out at the University of Tasmania (Supplementary Material Appendix 2). Zircons were extracted from three of the more differentiated rocks, a granophyre (DR10-16), a monzodiorite (DR11-6), and a rhyolite (DR12-29). The zircons extracted from the three rocks are euhedral (some unbroken grains with both terminations; others are stubby) and are 50-120 □m in length. In cathodoluminescence images, all analysed grains show oscillatory or sector zoning (Supplementary Fig. A3-1). Some grains in monzodiorite DR11-6 show igneous resorption textures on their margins. There are no identifiable inherited cores or metamict textures. U contents vary widely (31-1923 ppm) and Th/U is typically >1 (0.98-10.10). The Pb-U isotopic results define indistinguishable lower intercept ages for the three populations: 131.8±3.9 Ma (granophyre DR10-16), 128.2±2.3 Ma (monzodiorite DR11-6) and 129.8±6.1 Ma (rhyolite DR12-29, all ages ±2□, Fig.3).

5.2 $^{40}Ar/^{39}Ar$ dating of basaltic plagioclase

Three basaltic samples with well-preserved plagioclase were selected for $^{40}Ar/^{39}Ar$ dating. Basalt DR11-19 contains plagioclase phenocrysts ≤5 mm long in a grey groundmass; dolerite DR12-8 has plagioclase <1 mm long set in a mid-brown groundmass; and dolerite DR13-33 has plagioclase phenocrysts ≤15 mm long set in a light-brown groundmass. A description of the analytical methods and results is presented in Supplementary Material Appendix 3.

Plagioclases from DR11-19 and DR12-8 yield precise plateau ages of 129.4±1.3 and 130.6±1.2 Ma (2□), respectively, reflecting their relatively high K/Ca ratios and radiogenic ^{40}Ar yields (Fig.4). DR13-33 yields a plateau age of 130±4 Ma (2□), with the inferior age precision reflecting smaller sample size, lower K/Ca and lower radiogenic ^{40}Ar yields. The step-heating sequences for both DR11-19 and

DR12-8 show declining $\%^{40}Ar^*$ values at high temperature, reflecting increased atmospheric argon contributions from the resistance furnace itself; however this has no influence on the derived $^{40}Ar/^{39}Ar$ ages.

Initial $^{40}Ar/^{36}Ar$ ratios on isochron diagrams (Fig.4) are within error of modern-day atmospheric Ar, indicating the analysed plagioclase samples are free from inherited argon. While the low-temperature steps yield younger ages - attributed here to argon loss caused by incipient seawater alteration of the plagioclase - the reported plateau $^{40}Ar/^{39}Ar$ ages are based on 64 to 82% of the ^{39}Ar released, indicating they are reliable determinations of plagioclase crystallization ages. This is supported by concordant $^{40}Ar/^{39}Ar$ isochron and plateau ages.

The U-Pb zircon and $^{40}Ar/^{39}Ar$ plagioclase ages overlap within their reported uncertainties and range from 131.8±3.9 to 128.2±2.3 Ma, placing volcanic activity in this sector of the plateau in the late Hauterivian to Barremian, possibly just post-dating the ~132 Ma Valanginian-Hauterivian regional unconformity (Maloney et al., 2011).

6. Geochemistry

Concentrations of major and trace elements in 47 samples of basalts, dolerites, rhyolite and granophyre were determined by X-Ray fluorescence (XRF) and solution-mode ICP-MS (University of Tasmania), and are reported in Tables 2 to 4. Sr-Nd-Pb-Hf isotopic compositions were measured by multi-collector ICP-MS (University of Melbourne) and are reported in Table 5. Details of the analytical methods can be found in Appendices 2 and 5 (Supplementary Material).

6.1 Major Elements

The dredge samples from the Southern Surveyor 2005 cruise analysed here vary widely in composition (48.0 - 75.5 wt.% SiO_2, 0.16 to 7.3 wt.% MgO, Table 2). Loss on Ignition (LOI) ranges from 0.82 to 7.25 wt%, with only 6 of the 46 analysed samples having <2% LOI (Table 2). LOI is a broad measure of low-temperature alteration, and these results illustrate the extent of seawater alteration in the samples. Ca, Na and K are particularly mobile during submarine alteration (e.g. Hart et al., 1974) and their concentrations in the dredge samples are thus unlikely to be primary.

All mafic samples have <8% MgO (most have 5-7% MgO and 48-53% SiO_2, Fig.5a) indicating they represent relatively evolved magmas. The most differentiated members of this group have 2-4% MgO and up to 56% SiO_2. Al_2O_3 is high compared to many other basaltic suites (13 samples with >18 wt%, see Table 2), and CaO/Al_2O_3 is low (<0.6) in most analysed samples. This may reflect accumulation of Al-rich plagioclase (Bryan et al., 1981), consistent with prominent plagioclase phenocrysts in the lavas. Although there is much scatter (perhaps partly related to Ca mobility), CaO/Al_2O_3 tends to be lower at low MgO and approaches zero in the most silicic samples (DR10-16 and 12-41) and in DSDP Site 264 core material. In addition to plagioclase, a Ca-rich mineral - probably clinopyroxene - must have been an important fractionating phase. TiO_2 (0.79-3.41 wt.% in basaltic samples) shows a broad anti-correlation with MgO (Fig.5b). Low TiO_2 (<0.3%) in the four SiO_2-rich lavas indicates fractionation of a Fe-Ti oxide; the high magnetic susceptibilities recorded for the mafic samples suggest this is probably Ti-magnetite.

The most silicic samples analysed here have ~75% SiO_2, low Fe, Mg and Ca, and high Na and K (Table 2, Fig.5a, c). Silicic samples were also recovered at DSDP Site 264 (Coleman et al., 1982).

6.2 Trace Elements

Trace element concentrations (Tables 3, 4) show variations typical of basaltic systems: most incompatible elements (Zr, Nb, Hf, Ta, REE, Y, Th, U, Rb, Ba, Pb) are anti-correlated with Mg while Cr, Ni, Cu and Co show positive correlations. Many trends are scattered, undoubtedly reflecting alteration effects (Fig.6a). Co-variations among alteration-resistant elements (e.g. Nb, Zr, LREE) show much less scatter (Fig.6b, c). However, given the large geographic spread of the dredge samples, primary variations of trace element abundances, as well as local differentiation effects, probably contribute to the observed scatter.

The composition of mafic rocks varies with tectonic setting and the degree of partial melting; high degrees of partial melting typically produce tholeiitic magmas that are relatively depleted in incompatible elements while low degrees of melting typically produce alkaline magmas that are enriched in incompatible elements. To determine the relative extent of melting, it is important to determine if the Naturaliste Plateau dredge samples are tholeiitic or alkaline. Classification using the total alkalis (Na_2O+K_2O) versus SiO_2 diagram (TAS, Le Bas et al., 1986) is compromised by seawater alteration, and the results of a TAS classification (18 of the 45 dredge samples plot in the alkaline field, Fig. 5c) are likely to be spurious. An alternative subalkaline vs alkaline classification can be made using the alteration-resistant high field strength elements (Pearce and Cann, 1973), such as the Nb/Y ratio (Pearce and Norry, 1979), which identifies the Naturaliste Plateau samples as dominantly tholeiitic (Fig.5d).

Rare-earth element (REE) concentrations for 15 samples from eight of the nine sampled dredges are anti-correlated with MgO and have unfractionated to LREE-enriched normalized distribution patterns (Fig.7a), with La/Lu_{PM} ranging from 1.28 to 7.24 in the basalts and from 4.5 to 11.3 in two silicic rocks (Table 4, subscript 'PM'

denotes primitive mantle-normalized values, relative to values in McDonough and Sun, 1995). HREE fractionation is modest (Gd/Lu_{PM} 1.0-2.4). Some of the basaltic samples have patterns resembling those typical of Indian Ocean MORB while others match the patterns in Kerguelen Plateau basalts from ODP Site 1138 that have been proposed as melts derived from the hotspot at ~100 Ma (Neal et al., 2002).

Eu/Eu* (0.79-1.21 in the basalts, 0.36-0.54 in the silicic rocks) varies considerably and is undoubtedly controlled by plagioclase fractionation (viz. petrographic evidence and correlation with Al_2O_3). However, correlation with other parameters (e.g. La/Sm, Zr and radiogenic isotopes) suggest further controls, such as addition of a crustal component in some samples.

6.3 Sr-Nd-Pb-Hf isotopes

The radiogenic isotope compositions (Table 5) for nine of the least altered samples representing seven of nine dredges are highly heterogeneous. For example, parent/daughter ratios in eight basalts vary widely ($^{87}Rb/^{86}Sr$ 0.03-1.13, $^{147}Sm/^{144}Nd$ 0.139-0.203, $^{176}Lu/^{177}Hf$ 0.012-0.028, $^{238}U/^{204}Pb$ 2.2-20.9, $^{232}Th/^{204}Pb$ 9.4-54.9, Table 5). The respective values in rhyolite 12-41 are 3.65, 0.111, 0.0120, 4.6 and 79.9. The measured isotopic ranges for the basalts are: $^{87}Sr/^{86}Sr$ 0.7038 to 0.7147, ε_{Nd} +4.4 to -10.6, ε_{Hf} +4.7 to -15.7, $^{206}Pb/^{204}Pb$ 17.28 to 18.32 and $^{208}Pb/^{204}Pb$ 38.15 to 39.24 (Table 5). After age correction to 130 Ma, the average of the U-Pb zircon and plagioclase $^{40}Ar/^{39}Ar$ ages obtained here, $^{87}Sr/^{86}Sr_i$, $^{143}Nd/^{144}Nd_i$ and $^{176}Hf/^{177}Hf_i$ in the mafic rocks range from 0.7036 to 0.7135, 0.51268 to 0.51197 (ε_{Nd} +4.3 to -9.7) and 0.28291 to 0.28231 (ε_{Hf} +7.2 to -14.1), respectively (Table 5). These isotopic compositions show consistent correlations with each other and with chemical indices of differentiation, e.g. Si, Mg, Ti, and Zr concentrations (Figs.5, 6). While we will

argue below that this reflects crustal contamination, it also indicates that calculated $^{87}Sr/^{86}Sr_i$ ratios in the acid-leached samples are good estimates of primary $^{87}Sr/^{86}Sr$, despite the alteration experienced by the samples. Initial isotope ratios in rhyolite DR12-41 ($^{87}Sr/^{86}Sr_i$ 0.7175, ε_{Nd} -15.8, ε_{Hf} -18.8) extend the trends on Sr-Nd-Hf isotope plots and in plots of Sr-Nd-Hf isotopes versus Si, Mg and Zr, but not Ti, probably because Ti is strongly fractionated in the parental magmas of the most felsic rocks (Fig.5).

Initial Pb isotope ratios ($^{206}Pb/^{204}Pb$ 17.23-18.26, $^{207}Pb/^{204}Pb$ 15.58-15.68, $^{208}Pb/^{204}Pb$ 37.94-38.92, Table 5, Fig.8) do not show strong correlations with each other, with Sr-Nd-Hf isotopes, or with chemical parameters, despite the relatively modest age corrections ($^{206}Pb/^{204}Pb \leq 0.12$ and $^{208}Pb/^{204}Pb < 0.30$ in eight of nine samples). This lack of correlation suggests that either alteration effects are not sufficiently removed by the strong acid leaching of the analysed rock chips, and/or that primary Pb isotope variations were heterogeneous.

The large ranges in Sr-Nd-Hf isotopic ratios and their correlations with chemical compositions (Figs.5, 6, 8), as well as trace element evidence (high ratios of Th/Nb and La/Nb in the mafic rocks (Figs.7), and the geological setting of the ca. 130 Ma volcanic rocks on attenuated older continental crust, strongly indicate these results reflect a crustal contamination trend. This trend, defined by the mafic rocks, appears to be controlled by the same crustal component that is even more strongly expressed in the coeval rhyolite, DR12-41. Simple binary mixing lines between model mantle- and crustally-derived end-members (Fig. 8, details for end-members in figure caption) encompass, or pass close to, the data for the southern Naturaliste Plateau, and all other data sets plotted in these figures. The crustal end-member is based on published data for the Albany Fraser Orogen in southern Western Australia (Rosman et al., 1980;

Fletcher et al., 1983; Kirkland et al., 2011), which was considered the most likely onshore equivalent of granites and granitic gneisses recovered from the same *Southern Surveyor* dredges that yielded the basaltic material discussed here (Halpin et al., 2008). ε_{Nd} in the crustal end-member is based on the average of a large Nd isotope data set for the Albany Fraser Orogen (H. Smithies, pers.comm., augmented by data from Fletcher et al., 1983, ε_{Nd130} -19±5, ±1s, n = 70). ε_{Hf} is based on zircon-Hf isotope data reported in Kirkland et al. (2011). For our purpose, the initial $^{176}Hf/^{177}Hf$ recorded in the dated magmatic zircons (~1.35, 1.65-1.75 Ga) were 'aged' to 130 Ma using an average crustal $^{176}Lu/^{177}Hf$ of 0.015 (Goodge and Vervoort, 2006), to yield a range of ε_{Hf130} of -17 to -26. $^{87}Sr/^{86}Sr$ in the Albany Fraser Orogen is more difficult to estimate because strong heterogeneity is likely and because there are few published data. $^{87}Sr/^{86}Sr_{130}$ ratios for Meso- to Neoproterozoic granites and sedimentary rocks in the western part of the orogen (Rosman et al., 1980; Turek and Stephenson, 1966) are very high (>0.740), consistent with simple modelling of Rb-rich rocks of this age; we chose a $^{87}Sr/^{86}Sr_{130}$ of 0.74 for the model crustal end-member.

While the particular end-member compositions used here may not be representative or unique, they are plausible within the regional geological context and fit the data reasonably well. Based on the models, up to 70-75% of the Hf and Nd in rhyolite DR12-41 could be crustally derived. The least-contaminated samples, with positive ε_{Nd}-ε_{Hf} and $^{87}Sr/^{86}Sr$ of 0.7036-0.7046, contain <10% of the model crustal end-member. We note that data for basalts from the northern Naturaliste Plateau, from the onshore Bunbury and Rajmahal basalts, and for Cretaceous basalts from the Kerguelen Plateau and Broken Ridge are equally well described by these simple mixing curves, despite their very different geological locations.

The Sr-Nd isotope data for basalts dredged from the northern Naturaliste Plateau (Eltanin Cruise, 'NNP' in Fig.8) resemble those for the southern margin rocks (Figs. 8) but Pb isotope data follow different trends, with some samples close to the field for modern MORB from the Southeast Indian Ridge (Figs.8c, d).

7 Discussion

7.1 Comparison of Naturaliste Plateau basalt with the Bunbury Basalt in southwest Australia

The compositions of mafic rocks from the Naturaliste Plateau and those from the near-coeval on-shore Bunbury Basalt overlap substantially, despite the much more limited compositional range of the on-shore basalts (Figs. 5, 6, 7). Both suites show variable upper crustal signatures, e.g. in the Th/Nb vs. La/Nb plot (Fig. 7) where all samples lie on a trend from primitive mantle towards the composition of average upper continental crust, with Naturalist Plateau rhyolite DR12-41 showing the highest Th/Nb and La/Nb ratios. Mafic rocks dredged by USNS *Eltanin* from Site 55-12 on the northwest margin of the Naturaliste Plateau (Coleman et al., 1982) (Fig. 1) are similarly evolved, and those basalts less enriched in cumulus plagioclase phenocrysts show also high SiO_2 (mainly 54-57%), like the more fractionated among our dredged Naturaliste Plateau basalts. Mahoney et al. (1995) found that the *Eltanin* basalts have flat to slightly LREE-enriched REE patterns, like those from the southern margin of the Naturaliste Plateau, and they show similar large ranges in Th/Nb and La/Nb (Fig. 7).

The overlap in age (137-130 Ma vs. ~130 Ma) and composition strongly imply a spatial continuity between the Bunbury Basalts and basaltic rocks from the southern margin of the Naturaliste Plateau. Although undated, available geochemical data

suggest that it is also likely that the mafic samples dredged from USNS *Eltanin* on the northwest margin of the Naturaliste Plateau are part of the same magmatic province, as suggested by Mahoney et al. (1995).

7.2 Comparison between the Naturaliste and Kerguelen Plateaus

Cretaceous basaltic rocks from the Naturaliste Plateau (and from the onshore Bunbury Basalt) generally have higher SiO_2 contents (50-60 wt%) than basalts from the Kerguelen Plateau (e.g. ODP Site 1138, 45-50%, Fig.5). However, evolved compositions like those from the Naturaliste Plateau also occur on the Kerguelen Plateau, e.g. dacite forms the uppermost flow drilled at ODP Site 1138 (ref). Apparently as construction of the two igneous plateaus terminated, the flux of mantle-derived basaltic magma slowed sufficiently to enable formation of SiO_2-rich magma. Plagioclase-rich rocks like those found on the Naturaliste Plateau are also dominant at ODP Site 757 on the Ninetyeast Ridge (Frey et al., 1991). TiO_2 concentrations in Naturaliste Plateau basaltic rocks scatter strongly, reaching both lower and higher levels than those recorded at ODP Sites 1138 and 738 (Fig.5).

Isotopic (Sr-Nd-Pb-Hf) data for several tholeiitic mafic suites from the Kerguelen Plateau show trends towards evolved signatures similar to old continental crust. These include sites on the southern Kerguelen Plateau (ODP Site 738), from Elan Bank (ODP Site 1137) and from its conjugate margin, Broken Ridge (R/V *Conrad* dredge 8; Davies et al., 1989; Storey et al., 1992; Mahoney et al., 1995; Frey et al., 2002; Coffin et al., 2002; Ingle et al., 2002a, b, 2004). Mahoney et al. (1995) argued that these isotopic signatures signal 'shallow-level incorporation of continental lithosphere in either the head of the early Kerguelen plume or in plume-derived magmas' at 'sites located closest to rifted continental margins'. The strong continental

lithospheric signature observed in the Cretaceous dredge samples from the southern Naturaliste Plateau, like that observed in the Bunbury Basalt (Frey et al. 1996), supports this argument. Furthermore, the correlations of some major and trace elements with isotopic compositions (Figs. 5, 6) in the southern Naturaliste Plateau samples strongly indicate that the continental signature in these rocks was acquired at crustal level. The large geographic spread of the dredge samples and their strongly variable chemical-isotopic compositions (even within the same dredge, see data for DR7 and DR12, Table 5) imply they represent broadly coeval but spatially separate volcanic centres, each with its own magmatic history but involving the same (or similar) juvenile and crustal components (Fig. 8). The presence of exhumed lower continental crystalline Mesoproterozoic crust beneath the volcanic carapace of the Naturaliste Plateau (Halpin et al., 2008) and other sectors of offshore Western Australia (Williams et al., 2013), provides a suitable setting and obvious source for the inferred crustal component in the Cretaceous basalts. This is illustrated in Fig.9, which shows the isotope data of Fig.8 with some inferred source components (see also Ingle et al., 2003). In Hf-Pb isotope space (Fig.9a), for example, the southern Naturaliste Plateau basalts appear to be dispersed between the putative Kerguelen plume head component and a lower crustal component. Local granite gneisses from the same *Southern Surveyor* dredges have suitable compositions to represent this crustal source. The radiogenic Pb data (Fig.9b) are more difficult to interpret in terms of the mantle source (or sources involved) but a Lower Crust component (generally thought to be associated with low $^{206}Pb/^{204}Pb$, see Ingle et al., 2002) is again implied by the data trend. The *Southern Surveyor* gneiss samples shown in Fig.9a no longer provide a suitable match to the crustal component in the southern Naturaliste Plateau (SNP) basalts, as their $^{208}Pb/^{204}Pb$ is far too high. The crustal basement of the

Naturaliste Plateau thus is likely to be very heterogeneous, in particular in its Sr-Pb isotope composition.

7.3 A rift-fragmented Large Igneous Province in the Eastern Indian Ocean

Extensive dredging and geochronology from R/V *Southern Surveyor* cruise SS09/2005, together with seismic reflection data (Borissova, 2002; Maloney et al., 2011), potential field analyses (Direen et al., 2007), and DSDP data (Burkle et al., 1967; Ford, 1975) indicate that an extensive post-Valanginian volcanic carapace erupted over the Naturaliste Plateau and the adjacent Mentelle Basin (Maloney et al., 2011). This volcanic carapace formed a major unconformable landscape surface correlative with a similar surface in the Perth Basin, where it has also been drilled and dated (Dadd et al., 2015; Gorter and Deighton, 2002; Bradshaw et al., 2003). Above this surface are developed major, kilometre thick, seismically reflective, high velocity mounded edifices (Maloney et al., 2011), likely to be mafic volcanoes (Gorter and Deighton, 2002).

The discovery of major Cretaceous basaltic volcanism mantling the Naturaliste Plateau (this study) greatly expands the known volume of ~130 Ma basaltic volcanism in the eastern and northern margins of the wider Indian Ocean basin (Frey et al., 1996; Coffin et al., 2002; Duncan, 2002; Ingle et al., 2004; Zhu et al., 2008; Olierook et al., 2016). The area of the Naturaliste Plateau over which this Early Cretaceous volcanic surface has been encountered is ~90,000 km^2 (this study, Fig.1). Additional extensive early Cretaceous basaltic volcanism within the Australian region (Fig.1) that can be correlated to the Naturaliste Plateau in both age and composition occurs in the Mentelle Basin (see above, ~44,000 km^2, Maloney et al., 2011) and the ~124 Ma Wallaby Plateau (~70,000 km^2, Olierook et al., 2015); the onshore 137-130 Ma Bunbury Basalts of the Perth Basin (Olierook et al., 2016) cover

a relatively small area. Elsewhere, additional correlatives include ~40,000 km^2 of the Comei-Cona basalt suites in Tibet (Zhu et al., 2008, 2009), the Valanginian volcanic sectors of the Enderby Basin (Stagg et al., 2004), and the Princess Elizabeth Trough (Stagg et al., 2006) on the Antarctic Plate. Together, these geochemically similar 136-124 Ma basaltic volcanics cover a minimum total area of ~244,000 km^2. Assuming a thickness of 0.5-1 km (Frey et al., 1996; Direen et al., 2007; Zhu et al., 2008, 2009; Maloney et al., 2011), the minimum erupted volume is ~1.2 x 10^6 km^3, establishing the 137-124 Ma Naturaliste-Bunbury-Wallaby-Comei-Cona-Enderby-Antarctic province as a LIP in its own right (Coffin and Eldholm, 1992).

Geochemical and isotopic data (e.g. Davies et al., 1989; Storey et al., 1992; Mahoney et al., 1995; Frey et al., 1996, 2002; Kent et al., 1997, 2002; Neal et al., 2002; Duncan, 2002; Ingle et al., 2002a,b, 2003, 2004; Zhu et al., 2008; 2009; this study) indicate similarities between these ~130 Ma magmatic rocks and the oldest eruptive phases in the Kerguelen Plateau (ODP Site 1138: Coffin et al., 2002). Perhaps the most noticeable shared feature is the occurrence of Nb-depleted basalts (Fig. 7d). A characteristic of the continental crust, Nb depletions are observed in Cretaceous basalts from ODP sites 738 and 1137 on the Kerguelen Plateau, in the Rajmahal Traps, Bunbury Basalt, Wallaby Basin and on the Naturaliste Plateau.

8. Conclusions

Similarities in age, major and trace element composition, and Sr-Nd-Hf-Pb isotopic ratios in the now widely dispersed fragments of early Kerguelen hotspot magmatism, including rocks in southeast Tibet (Zhu et al., 2008, 2009), northeast India (Kent et al., 1997, 2002), southwest Western Australia (Frey et al., 1996; Ingle et al., 2004; Olierook et al., 2016), Wallaby Plateau (Olierook et al., 2015) and the Naturaliste

Plateau (this study) document LIP formation at 137-124 Ma. This LIP predates the earliest known stages recorded from the Kerguelen Plateau (~120 Ma: Coffin et al., 2002, Duncan, 2002) although we note that the currently deepest penetration of Kerguelen Plateau igneous basement is only 233 m of an estimated ~20 km total thickness (Coffin et al., 2000); older Cretaceous eruptions may yet be found on the Kerguelen Plateau. The extensive layer-cake stratigraphy of the 0.5-1 km-thick seismically defined mafic cover of the Naturaliste Plateau (Borissova, 2002; Direen et al., 2007), and the absence of seaward-dipping reflector sequence crustal architecture that dominates the Australian margin north of the Wallaby-Zenith Fracture Zone (Planke et al., 2000; Direen et al., 2008), indicates that this plateau and the adjacent Mentelle Basin represent a ~130,000 km^2 fragment of the Kerguelen LIP, rather than breakup-related volcanism at the margin of continental plates.

If the extensive basaltic volcanism on the Naturaliste Plateau and Mentelle Basin is indeed an early stage of the Kerguelen hotspot volcanism, models involving an "incubating plume" (Kent et al., 1992; Coffin et al., 2002; Zhu et al., 2008, 2009; Ingle et al., 2002, 2004) are no longer necessary to explain the apparent age difference between this magmatic activity and the oldest known volcanism on the Kerguelen Plateau. It also confirms that the Kerguelen hotspot did not trigger the contemporaneous continental breakup, even if correlation with the Naturaliste-Bunbury sequences now mean that its earliest recorded products could be as old as 137 Ma, because breakup was already underway and progressing from north (Mihut and Mueller, 1998; Direen et al., 2008) to south (Markl, 1978; Powell et al., 1988; Bradshaw et al., 2003) to southwest (Stagg et al., 2004; Gaina et al., 2007). The role of mantle plumes or hotspots as a trigger for breakup was also recently questioned for the South Atlantic Ocean (Fromm et al., 2015). Open questions remain about the

possible role of large plate-boundary-forming stresses related to rifting in the post-breakup formation of this LIP.

Acknowledgements

We thank Master Ian Taylor, the ship's crew, and the technical and scientific staff of R/V *Southern Surveyor* voyage SS09/2005. AJC acknowledges Australian Research Council (ARC) grant DP0666062, and financial support of the Major National Research Facility for the R/V *Southern Surveyor* cruise SS09/2005, as well as analytical support from Geoscience Australia. NGD acknowledges the support of FROGTECH Pty Ltd in pursuing this research during the period 2006-2013. The $^{40}Ar/^{39}Ar$ analyses were carried out at, and partially funded by, the UQ-AGES laboratory at The University of Queensland, and we gratefully acknowledge the support provided by P. Vasconcelos and D. Thiede. JMW acknowledges ARC grant DE150130. We thank K. Dadd and J. Foden for their reviews, and G. Caprarelli for editorial handling. An earlier version of this manuscript was improved by reviews from A. Kerr and an anonymous reviewer.

Table 1 *Southern Surveyor* SS09/05 Dredge location and contents

Table 2: Abundance of Major Elements (wt %)

Table 3: Abundance of Trace elements (ppm) Analyzed by X-Ray Fluorescence

Table 4: Abundance of Trace elements (ppm) Analyzed by ICP-MS

Table 5: Radiogenic (Sr-Nd-Hf-Pb) isotope compositions

References

Beslier, M.O., Royer, J.Y., Girardeau, J., Hill, P.J., Boeuf, E., Buchanan, C., Chatin, F., Jacovetti, G., Moreau, A., Munschy, M., Partouche, C., Robert, U., Thomas, S., 2004. Une large transition continent-ocean en pied de marge sud-ouest australienne: premiers resultats de la campagne MARGAU/MD110. Bulletin Societe geologique Francaise 175, 629-641.

Borissova, I., 2002. Geological framework of the Naturaliste Plateau. Geoscience Australia Record 2002/20.

Bradshaw, B.E., Rollet, N., Totterdell, J.M., Borissova, I., 2003. A revised structural framework for frontier basins on the southern and southwestern Australian continental margin. Geoscience Australia Record 2003/03.

Bryan, W.B., Thompson, G., Ludden, J.N., 1981. Compositional variation in normal MORB from 22°–25°N: Mid-Atlantic Ridge and Kane Fracture Zone. Journal of Geophysical Research: Solid Earth 86, 11815-11836.

Burkle, L.H., Saito, T., Ewing, M., 1967. A Cretaceous (Turonian) core from the Naturaliste Plateau. Deep-sea Research 14, 421-426.

Coffin, M.F., Eldholm, O., 1992. Volcanism and continental break-up; a global compilation of large igneous provinces, In: Storey, B.C., Alabaster, T., and Pankhurst R.J. (Eds.), Magmatism and the causes of continental break-up. Geological Society (London) Special Publications, London, United Kingdom, pp. 17-30.

Coffin, M.F., Frey, F.A., Wallace, P.J., et al., 2000. Proc. ODP, Init. Repts., 183 [Online]. Available from World Wide Web: http://www-odp.tamu.edu/publications/183_IR/183ir.htm.

Coffin, M.F., Pringle, M.S., Duncan, R.A., Gladczenko, T.P., Storey, M., Müller, R.D., Gahagan, L.A., 2002. Kerguelen Hotspot Magma Output since 130Ma. Journal of Petrology 43, 1121-1139.

Coleman, P.J., Michael, P.J., Mutter, J.C., 1982. The origin of the Naturaliste Plateau, SE Indian Ocean; implications from dredged basalts. Journal of the Geological Society of Australia 29 457-468.

Crawford, A.J., 2005. Voyage Summary SS09/2005. CSIRO, Hobart, 10 pp.

Dadd, K.A., Kellerson, L., Borissova, I. and Nelson, G., 2015. Multiple sources for volcanic rocks dredged from the Western Australian rifted margin. Marine Geology, 368, 42-57.

Davies, T.A., Luyendyk, B.P., Rodolfo, K.S., Kempe, D.R.C., McKelvey, B.C., Leidy, R.D., Horvath, G.J., Hydndmann, R.D., Thierstein, H.R., Herb, R.C., Boltovskoy, E., Doyle, P., 1974. Site 258, Initial Reports of the Deep Sea Drilling Program. U.S. Government Printing Office, Washington, pp. 359-414.

Davies, H.L., Sun, S.-S., Frey, F.A., Gautier, I., McCulloch, M.T., Price, R.C., Bassias, Y., Klootwijk, C., Leclaire, L., 1989. Basalt basement from the Kerguelen

Plateau and the trail of a Dupal plume. Contributions to Mineralogy and Petrology 103, 457 – 469.

Direen, N.G., Borissova, I., Stagg, H.M.J., Colwell, J.B., Symonds, P.A., 2007. Nature of the continent–ocean transition zone along the southern Australian continental margin: a comparison of the Naturaliste Plateau, SW Australia, and the central Great Australian Bight sectors, In: Karner, G.D., Manatschal, G., Pinheiro, L.M. (Eds.), Imaging, Mapping and Modelling Continental Lithosphere Extension and Breakup. Geological Society (London) Special Publications 282, pp. 235-261.

Direen, N.G., Stagg, H.M.J., Symonds, P.A., Colwell, J.B., 2008. Architecture of volcanic rifted margins: new insights from the Exmouth-Gascoyne margin, Western Australia. Australian Journal of Earth Sciences 55, 341-363.

Direen, N.G., 2011. Comment on "Antarctica — Before and after Gondwana" by S.D. Boger, Gondwana Research, Volume 19, Issue 2, March 2011, Pages 335–371. Gondwana Research 21, 302-304.

Direen, N.G., Stagg, H.M.J., Symonds, P.A., Colwell, J.B., 2011. Dominant symmetry of a conjugate southern Australian and East Antarctic magma-poor rifted margin segment. Geochemistry Geophysics Geosystems 12, 10.1029/2010gc003306.

Direen, N.G., Stagg, H.M.J., Symonds, P.A., Norton, I.O., 2013. Variations in rift symmetry: cautionary examples from the Southern Rift System (Australia-Antarctica), In: Mohriak, W.U., Danforth, A., Post, P.J., Brown, D.E., Tari, G.C., Nemčok, M., Sinha, S.T. (Eds.), Conjugate Divergent Margins Geological Society (London) Special Publication 369, pp. 453-475.

Duncan, R.A., 2002. A time frame for construction of the Kerguelen Plateau and Broken Ridge. Journal of Petrology 43, 1109-1119.

Fitton, J.G., Larsen, L.M., Saunders, A.D., Hardarson, B.S., Kempton, P.D., 2000. Palaeogene Continental to Oceanic Magmatism on the SE Greenland Continental Margin at 63°N: a Review of the Results of Ocean Drilling Program Legs 152 and 163. Journal of Petrology 41, 951-966.

Fleck, R. J., Sutter, J. F., and Elliot, D. H., 1977, Interpretation of discordant 40Ar/39Ar age-spectra of Mesozoic tholeiites from Antarctica: Geochimica et Cosmochimica Acta. 41, 15-32.

Ford, A.B., 1975. Volcanic rocks of Naturaliste Plateau, Eastern Indian Ocean, Site 264, DSDP Leg 28, In: Hayes, D.E., Frakes L.A., Barrett, P.J., Burns, D.A., Chen, P.-H., Ford, A.B., Kaneps, A.G., Kemp, E.M., McCollum, D.W., Piper, D.J.W., Wall, R.E., Webb, P.N. (Eds.), Initial Reports of the Deep Sea Drilling Project. U.S. Government Printing Office, Washington, pp. 821-833.

Frey, F., Jones, W., Davies, H., Weis, D., 1991. Geochemical and petrologic data for basalts from Sites 756, 757, and 758: implications for the origin and evolution of Ninetyeast Ridge, Proceedings of the Ocean Drilling Program Scientific Results, pp. 611-659.

Frey, F.A., McNaughton, N.J., Nelson, D.R., de Laeter, J.R., Duncan, R.A., 1996. Petrogenesis of the Bunbury Basalt, Western Australia: interaction between the Kerguelen plume and Gondwana lithosphere? Earth and Planetary Science Letters 144, 163-183.

Frey, F.A., Weis, D., Borisova, A.Y., Xu, G., 2002. Involvement of continental crust in the formation of the Cretaceous Kerguelen Plateau: New perspectives from ODP Leg 120 sites. Journal of Petrology 43, 1207-1239.

Fromm, T., Planert, L., Jokat, W., Ryberg, T., Behrmann, J.H., Weber, M., Haberland, C., 2015. South Atlantic opening: A plume-induced breakup? Geology 43, 931-934.

Gaina, C., Mueller, R.D., Brown, B., Ishihara, T., Ivanov, S., 2007. Breakup and early seafloor spreading between India and Antarctica. Geophysical Journal International 170, 151-169.

Goodge, J.W., Vervoort, J.D., 2006. Origin of Mesoproterozoic A-type granites in Laurentia: Hf isotope evidence. Earth and Planetary Science Letters 243, 711-731.

Gorter, J.D., Deighton, I., 2002. Effects of igneous activity in the offshore northern Perth Basin; evidence from petroleum exploration wells, 2D seismic and magnetic surveys, In: Keep, M., Moss, S.J. (Eds.), The Sedimentary Basins of Western Australia 3; Proceedings of the West Australian Basins Symposium. Petroleum Exploration Society of Australia. Perth, Western Australia, Australia.

Graham, D.W., Blichert-Toft, J., Russo, C.J., Rubin, K.H., Albarede, F., 2006. Cryptic striations in the upper mantle revealed by hafnium isotopes in southeast Indian Ridge basalts. Nature 440, 199-202

Halpin, J.A., Crawford, A.J., Direen, N.G., Coffin, M.F., Forbes, C.J., Borissova, I., 2008. Naturaliste Plateau, offshore Western Australia: a submarine window into Gondwana assembly and breakup. Geology 36, 807-810.

Hanan, B.B., Blichert-Toft, J., Hemond, C., Sayit, K., Agranier, A., Graham, D.W., Albarède, F., 2013. Pb and Hf isotope variations along the Southeast Indian Ridge and the dynamic distribution of MORB source domains in the upper mantle. Earth and Planetary Science Letters 375, 196-208.

Hart, S., Erlank, A., Kable, E., 1974. Sea floor basalt alteration: some chemical and Sr isotopic effects. Contributions to Mineralogy and Petrology 44, 219-230.

Hayes, D.E., Frakes L.A., Barrett, P.J., Burns, D.A., Chen, P.-H., Ford, A.B., Kaneps, A.G., Kemp, E.M., McCollum, D.W., Piper, D.J.W., Wall, R.E., Webb, P.N., 1975. Site 264, Initial Reports of the Deep Sea Drilling Project. U.S. Government Printing Office, Washington, pp. 821-833.

Heezen, B.C., Tharp, M., 1973. USNS *Eltanin* cruise 55. Antarctic Journal of the United States VIII, 137-141.

Ingle, S., Weis, D., Frey, F.A., 2002a. Indian continental crust recovered from Elan Bank, Kerguelen Plateau (ODP Leg 183, Site 1137). Journal of Petrology 43, 1241-1257.

Ingle, S., Weis, D., Scoates, J.S., Frey, F.A., 2002b. Relationship between the early Kerguelen plume and continental flood basalts of the paleo-Eastern Gondwanan margins. Earth and Planetary Science Letters 197, 35-50.

Ingle, S., Weis, D., Doucet, S., Mattielli, N., 2003. Hf isotope constraints on mantle sources and shallow-level contaminants during Kerguelen hotspot activity since 120 Ma. Geochemistry Geophysics Geosystems 4, 1068 doi: 1010.1029/2002GC000482.

Ingle, S., Scoates, J.S., Weis, D., Brugmann, G., Kent, R.W., 2004. Origin of Cretaceous continental tholeiites in southwestern Australia and eastern India: insights from Hf and Os isotopes. Chemical Geology 209, 83-106.

Jongsma, D., Petkovic, P., 1977. The structure of the Naturaliste Plateau and trough. The APEA Journal 17 Part 1, 3-12.

Kent, R.W., Pringle, M.S., Müller, R.D., Saunders, A.D., Ghose, N.C., 2002. ^{40}Ar / ^{39}Ar geochronology of the Rajmahal basalts, India and their relationship to the Kerguelen Plateau. Journal of Petrology 43, 1141-1153.

Kent, R.W., Saunders, A.D., Kempton, P.D., Ghose, N.C., 1997. Rajmahal basalts, eastern India: mantle sources and melt distribution at a volcanic rifted margin, In: Mahoney, J.J., Coffin, M.F. (Eds.), Large Igneous Provinces: Continental, Oceanic and Planetary Flood Volcanism. . American Geophysical Union Geophysical Monograph 100, pp. 145-182.

Kent, R.W., Storey, M., Saunders, A.D., 1992. Large igneous provinces: Sites of plume impact or plume incubation? Geology 20, 891-894.

Kirkland, C., Spaggiari, C., Pawley, M., Wingate, M., Smithies, R., Howard, H., Tyler, I., Belousova, E.A., Poujol, M., 2011. On the edge: U–Pb, Lu–Hf, and Sm–Nd data suggests reworking of the Yilgarn craton margin during formation of the Albany-Fraser Orogen. Precambrian Research 187, 223-247.

Le Bas, M.J., Le Maitre, R., Streckeisen, A., Zanettin, B., 1986. A chemical classification of volcanic rocks based on the total alkali-silica diagram. Journal of Petrology 27, 745-750.

Lee, J.-Y., Marti, K., Severinghaus, J. P., Kawamura, K., Yoo, H.-S., Lee, J. B., and Kim, J. S., 2006, A redetermination of the isotopic abundances of atmospheric Ar: Geochimica et Cosmochimica Acta. 70, 4507-4512.

Mahoney, J.J., Jones, W.B., Frey, F.A., Salters, V.J.M., Pyle, D.G., Davies, H.L., 1995. Geochemical characteristics of lavas from Broken Ridge, the Naturaliste Plateau and southernmost Kerguelen Plateau: Cretaceous plateau volcanism in the southeast Indian Ocean. Chemical Geology 120, 315-345.

Mahoney, J.J., Graham, D.W., Christie, D.M., Johnson, K.T.M., Hall, L.S., Vonderhaar, D.L., 2002. Between a hotspot and a cold spot: isotopic variation in the Southeast Indian Ridge astenosphere, 86oE-118oE. Journal of Petrology 43, 1155-1176

Maloney, D., Sargent, C., Direen, N.G., Hobbs, R.W., Grocke, D.R., 2011. Re-evaluation of the Mentelle Basin, a polyphase rifted margin basin, offshore south-west Australia: new insights from integrated regional seismic datasets. Solid Earth 2, 107-123.

Markl, R.G., 1978. Further evidence for the Early Cretaceous breakup of Gondwanaland off southwestern Australia. Marine Geology 26, 41-48.

McDonough, W.F., Sun, S.-S., 1995. The composition of the Earth. Chemical Geology 120, 223-253.

Mihut, D., Mueller, R.D., 1998. Volcanic margin formation and Mesozoic rift propagators in the Cuvier abyssal plain off Western Australia. Journal of Geophysical Research, B, Solid Earth and Planets 103, 27135-127149.

Mutter, J.C., Cande, S.C., 1983. The early opening between Broken Ridge and Kerguelen Plateau. Earth and Planetary Science Letters 65, 369-376.

Neal, C.R., Mahoney, J., Chazey, W., 2002. Mantle sources and the highly variable role of continental lithosphere in basalt petrogenesis of the Kerguelen Plateau and Broken Ridge LIP: results from ODP Leg 183. Journal of Petrology 43, 1177 – 1205.

Nicolaysen, K., Bowring, S., Frey, F., Weis, D., Ingle, S., Pringle, M.S., Coffin, M.F., Leg 183 Shipboard Scientific Party, 2001. Provenance of Proterozoic garnet-biotite gneiss recovered from Elan Bank, Kerguelen Plateau, southern Indian Ocean. Geology 29, 235-238.

Olierook, H.K., Merle, R.E., Jourdan, F., Sircombe, K., Fraser, G., Timms, N.E., Nelson, G., Dadd, K.A., Kellerson, L., Borissova, I., 2015. Age and geochemistry of magmatism on the oceanic Wallaby Plateau and implications for the opening of the Indian Ocean. Geology 43, 971-974.

Olierook, H.K., Jourdan, F., Merle, R.E., Timms, N.E., Kusznir, N., Muhling, J.R., 2016. Bunbury Basalt: Gondwana breakup products or earliest vestiges of the Kerguelen mantle plume? Earth and Planetary Science Letters 440, 20-32.

Pearce, J.A., Cann, J., 1973. Tectonic setting of basic volcanic rocks determined using trace element analyses. Earth and Planetary Science Letters 19, 290-300.

Pearce, J., Norry, M., 1979. Petrogenetic implications of Ti, Zr, Y, and Nb variations in volcanic rocks. Contributions to Mineralogy and Petrology 69, 33-47.

Péron-Pinvidic, G., Manatschal, G., 2009. The final rifting evolution at deep magma-poor passive margins from Iberia-Newfoundland: a new point of view. International Journal of Earth Sciences 98, 1581-1597.

Petkovic, P., 1975. Origin of the Naturaliste Plateau. Nature 253, 30-33.

Planke, S., Symonds, P.A., Alvestad, E., Skogseid, J., 2000. Seismic volcanostratigraphy of large volume basaltic extrusive complexes on rifted margins. Journal of Geophysical Research 105, 19,335-319,351.

Powell, C.M., Roots, S.R., Veevers, J.J., 1988. Pre-breakup continental extension in East Gondwanaland and the early opening of the eastern Indian Ocean. Tectonophysics 155, 261-283.

Rosman, K., Wilde, S., Libby, W., De Laeter, J., 1980. Rb-Sr dating of granitic rocks in the Pemberton area. Western Australian Geological Survey, Annual Report for 1979, 97-100.

Royer, J.Y., Coffin, M.F., 1992. Jurassic to Eocene plate tectonic reconstructions in the Kerguelen Plateau region, In: Wise Jr., S.W., Schlich, R. (Eds.), Proceedings of the Ocean Drilling Program, Scientific Results v. 120, pp. 917-928.

Rudnick, R.L., Gao, S., 2014. 4.1 - Composition of the Continental Crust A2 - Holland, Heinrich D, In: Turekian, K.K. (Ed.), Treatise on Geochemistry (Second Edition). Elsevier, Oxford, pp. 1-51.

Sayers, J., Symonds, P.A., Direen, N.G., Bernardel, G., 2001. Nature of the continent-ocean transition on the non-volcanic rifted margin of the central Great Australian Bight, In: Wilson, R.C.L., Whitmarsh, R.B., Taylor, B., Froitzheim, N. (Eds.), Non-volcanic rifting of continental margins; a comparison of evidence from land and sea. Geological Society (London) Special Publication 187, pp. 51-76.

Stagg, H.M.J., Colwell, J.B., Direen, N.G., O'Brien, P.E., Bernardel, G., Borissova, I., Brown, B.J., Ishihara, T., 2004. Geology of the continental margin of Enderby and Mac. Robertson Lands, East Antarctica: Insights from a regional data set. Marine Geophysical Researches 25, 183-219.

Stagg, H.M.J., Colwell, J.B., Borissova, I., Ishihara, T., Bernardel, G., 2006. The Bruce Rise Area, East Antarctica: Formation of a Continental Margin near the Greater India - Australia - Antarctica Triple Junction. Terra Antarctica 13, 3-22.

Storey, M., Kent, R.W., Saunders, A.D., Salters, V.J.M., Hergt, J., Whitechurch, H., Sevigny, J.H., Thirlwall, M.F., Leat, P., Ghose, N.C., Gifford, M., 1992. Lower Cretaceous volcanic rocks on continental margins and their relationship to the Kerguelen Plateau, In: Wise, S.W., Schlich, R., et al (Eds.), Proceedings of the Ocean Drilling Program, Scientific Results, College Station, Texas, pp. 33-47.

Tikku, A.A., Cande, S.C., 2000. On the fit of Broken Ridge and Kerguelen Plateau. Earth and Planetary Science Letters 180, 117-132.

Tikku, A.A., Direen, N.G., 2008. Comment on “Major Australian-Antarctic Plate Reorganization at Hawaiian-Emperor Bend Time”. Science 321, 490-491c.

Totterdell, J., Blevin, J., Struckmeyer, H., Bradshaw, B., Colwell, J., Kennard, J., 2000. Petroleum frontiers, systems and plays-A new sequence framework for the

Great Australian Bight: Starting with a clean slate. APPEA Journal-Australian Petroleum Production and Exploration Association 40, 95-120.

Turek, A., Stephenson, N., 1966. The radiometric age of the Albany Granite and the Stirling Range Beds, southwest Australia. Journal of the Geological Society of Australia 13, 449-456.

Veevers, J.J., Li, Z.X., 1991. Review of seafloor spreading around Australia. II. Marine magnetic anomaly modelling. Australian Journal of Earth Sciences 38, 391-408.

White, W., Klein, E., 2014. 4.13-Composition of the Oceanic Crust. Treatise on Geochemistry (Second Edition).

Williams, S.E., Whittaker, J.M., Granot, R., Mueller, R.D., 2013. Early India-Australia spreading history revealed by newly detected Mesozoic magnetic anomalies in the Perth Abyssal Plain. Journal of Geophysical Research 118, 1-10.

Zhu, D., Mo, X., Pan, G., Zhao, Z., Dong, G., Shi, Y., Liao, Z., Wang, L., Zhou, C., 2008. Petrogenesis of the earliest Early Cretaceous mafic rocks from the Cona area of the eastern Tethyan Himalaya in south Tibet: Interaction between the incubating Kerguelen plume and the eastern Greater India lithosphere? Lithos 100, 147-173.

Zhu, D.-C., Chung, S.-L., X.-X., M., Zhao, Z.-D., Niu, Y., Song, B., Yang, Y.-H., 2009. The 132 Ma Comei-Bunbury large igneous province: Remnants identified in present-day southeastern Tibet and southwestern Australia. Geology 37, 583-586.

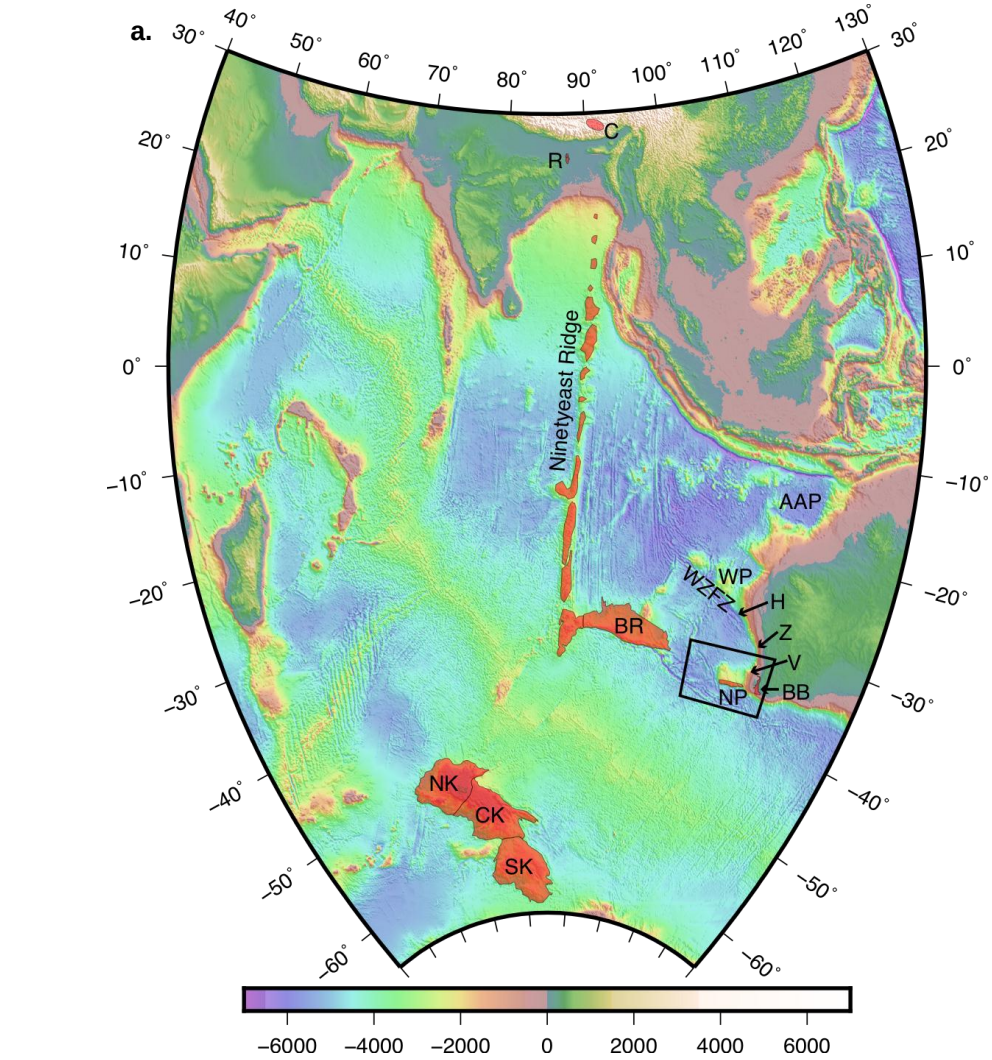

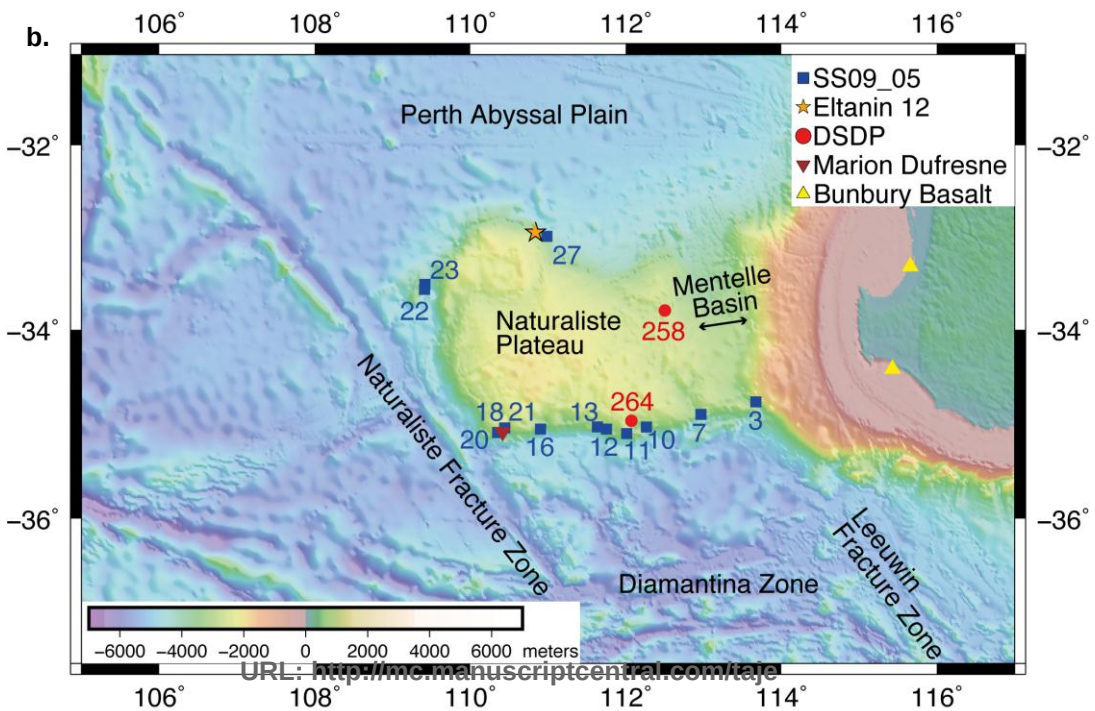

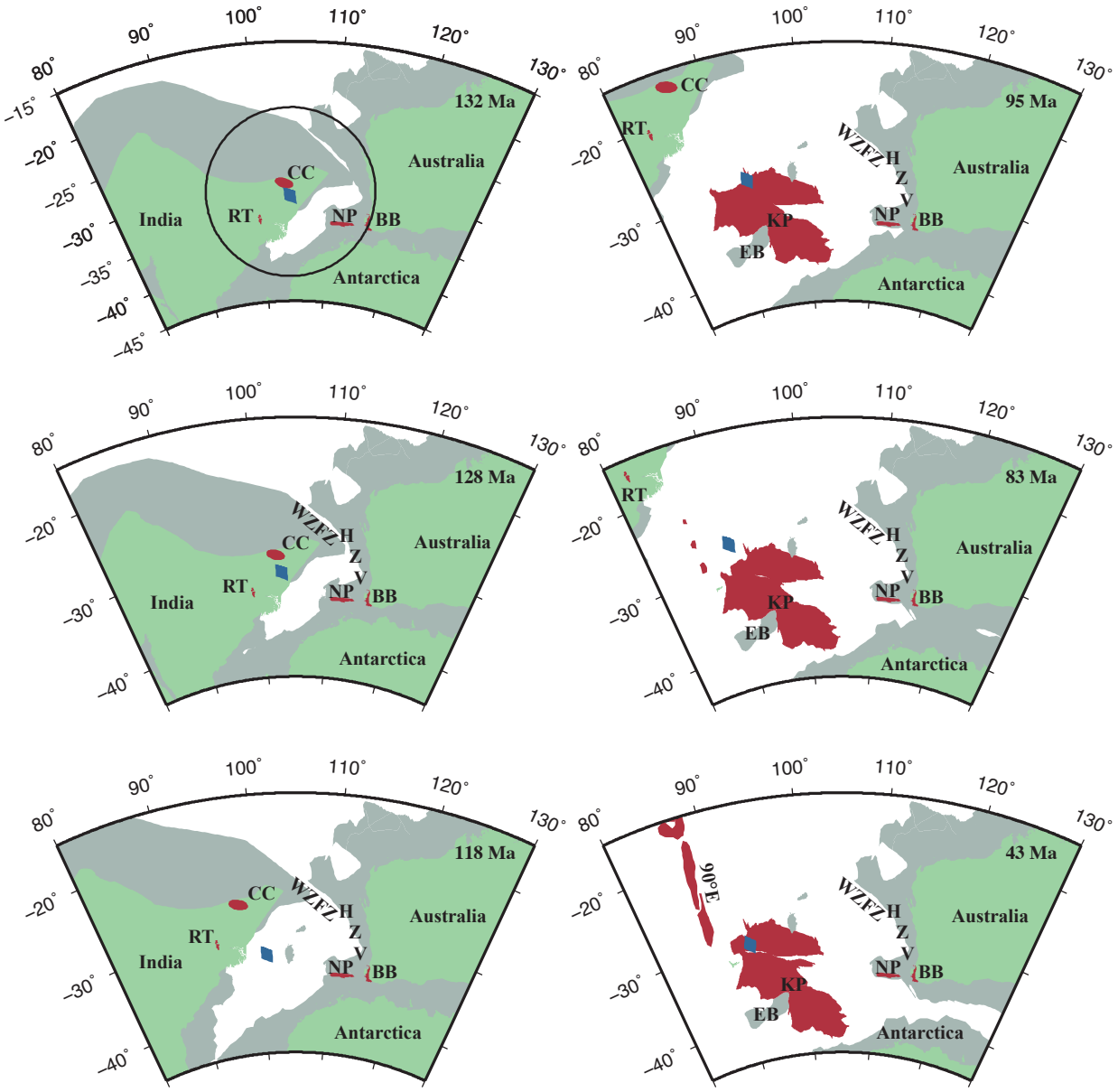
132 Ma
95 Ma
128 Ma
83 Ma
118 Ma
43 Ma
India
Australia
Antarctica
CC
RT
NP
BB
WZFZ
H
Z
V
KP
EB
90°E

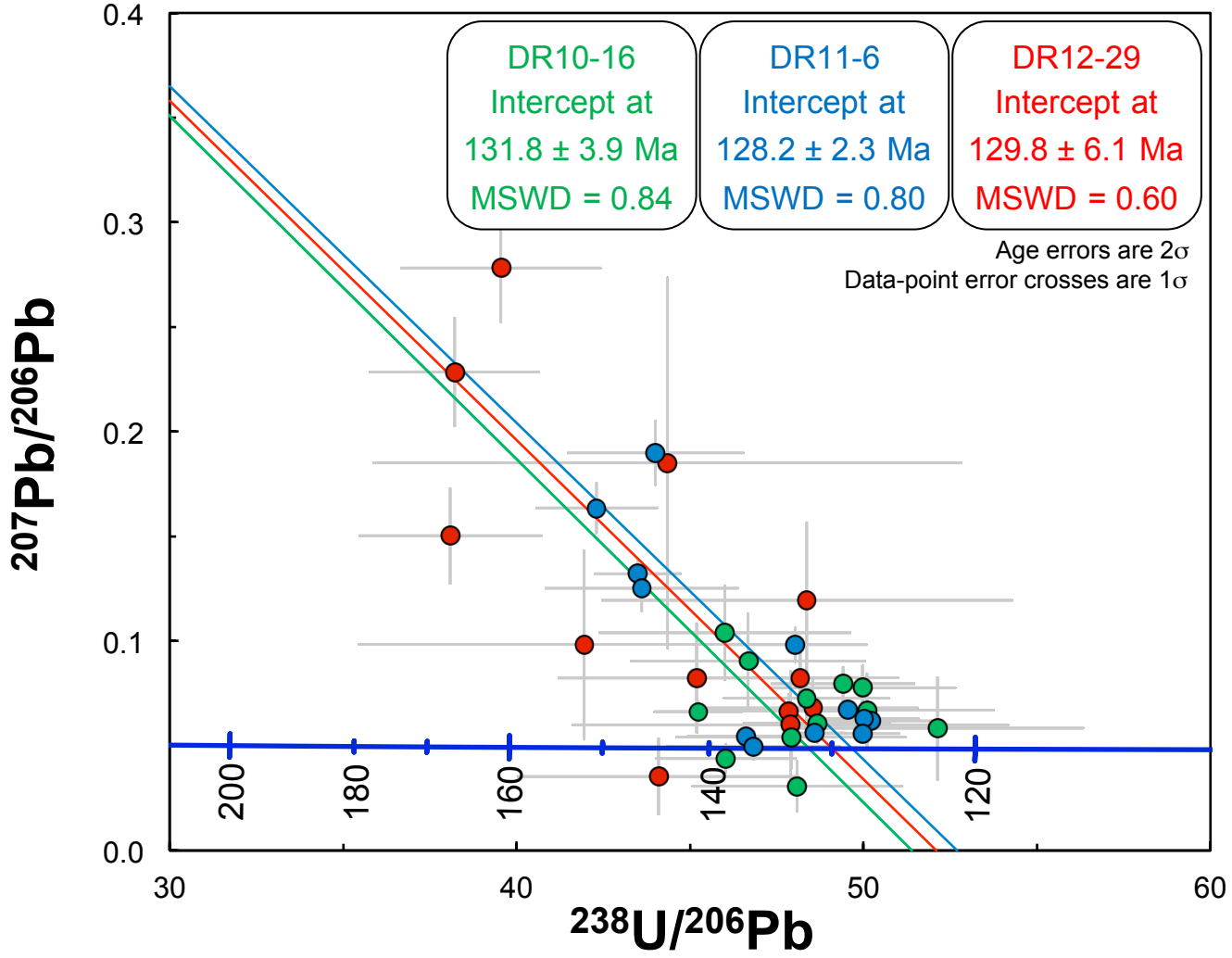
DR10-16
Intercept at
131.8 ± 3.9 Ma
MSWD = 0.84
DR11-6
Intercept at
128.2 ± 2.3 Ma
MSWD = 0.80
DR12-29
Intercept at
129.8 ± 6.1 Ma
MSWD = 0.60
Age errors are 2σ
Data-point error crosses are 1σ
0.4
0.3
0.2
0.1
0.0
30
40
50
60
200
180
160
140
120
207Pb/206Pb
238U/206Pb

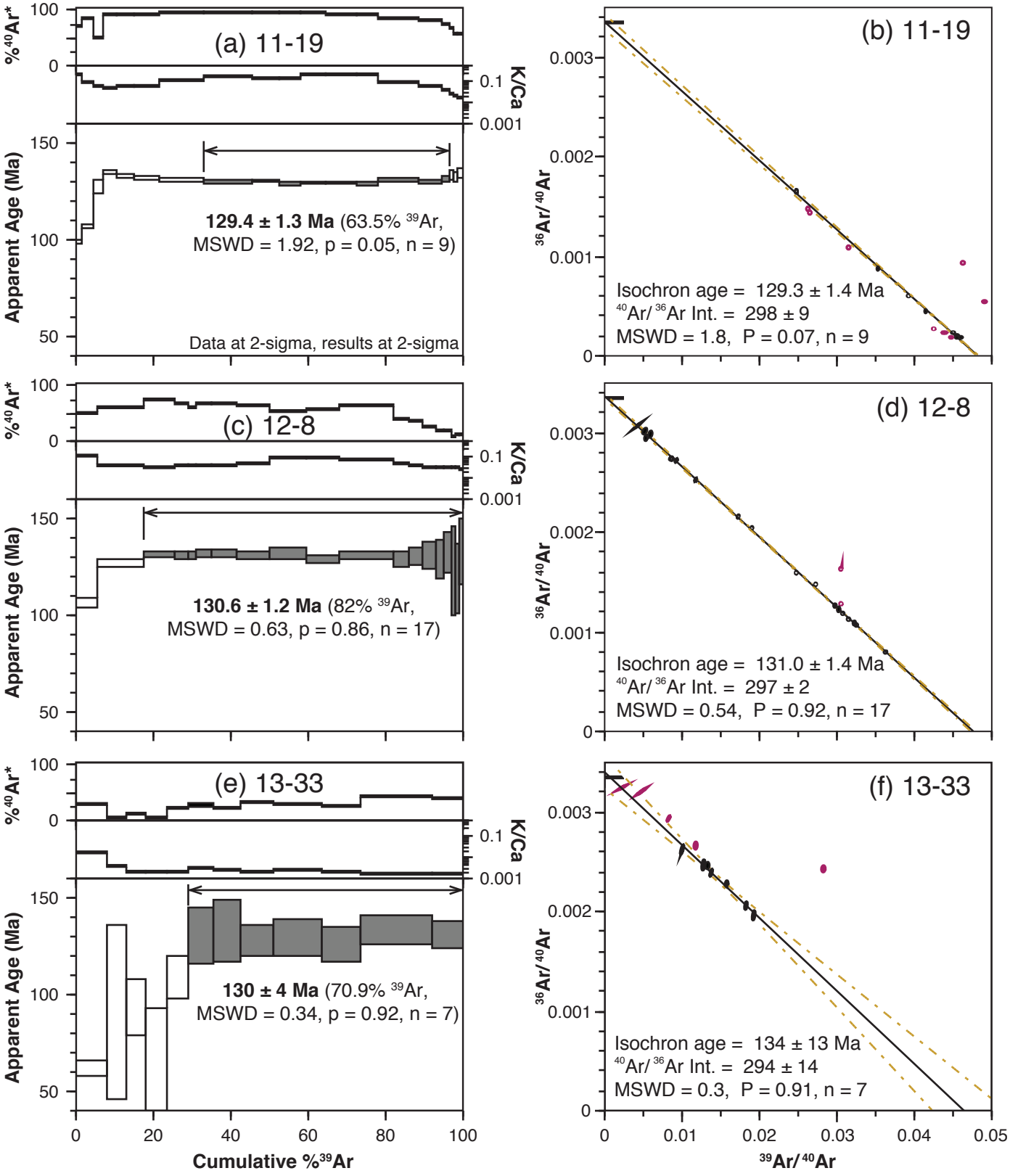
(a) 11-19
%40Ar*
K/Ca
Apparent Age (Ma)
129.4 ± 1.3 Ma (63.5% 39Ar,
MSWD = 1.92, p = 0.05, n = 9)
Data at 2-sigma, results at 2-sigma
(b) 11-19
36Ar/40Ar
Isochron age = 129.3 ± 1.4 Ma
40Ar/36Ar Int. = 298 ± 9
MSWD = 1.8, P = 0.07, n = 9
(c) 12-8
130.6 ± 1.2 Ma (82% 39Ar,
MSWD = 0.63, p = 0.86, n = 17)
(d) 12-8
Isochron age = 131.0 ± 1.4 Ma
40Ar/36Ar Int. = 297 ± 2
MSWD = 0.54, P = 0.92, n = 17
(e) 13-33
130 ± 4 Ma (70.9% 39Ar,
MSWD = 0.34, p = 0.92, n = 7)
Cumulative %39Ar
(f) 13-33
Isochron age = 134 ± 13 Ma
40Ar/36Ar Int. = 294 ± 14
MSWD = 0.3, P = 0.91, n = 7
39Ar/40Ar

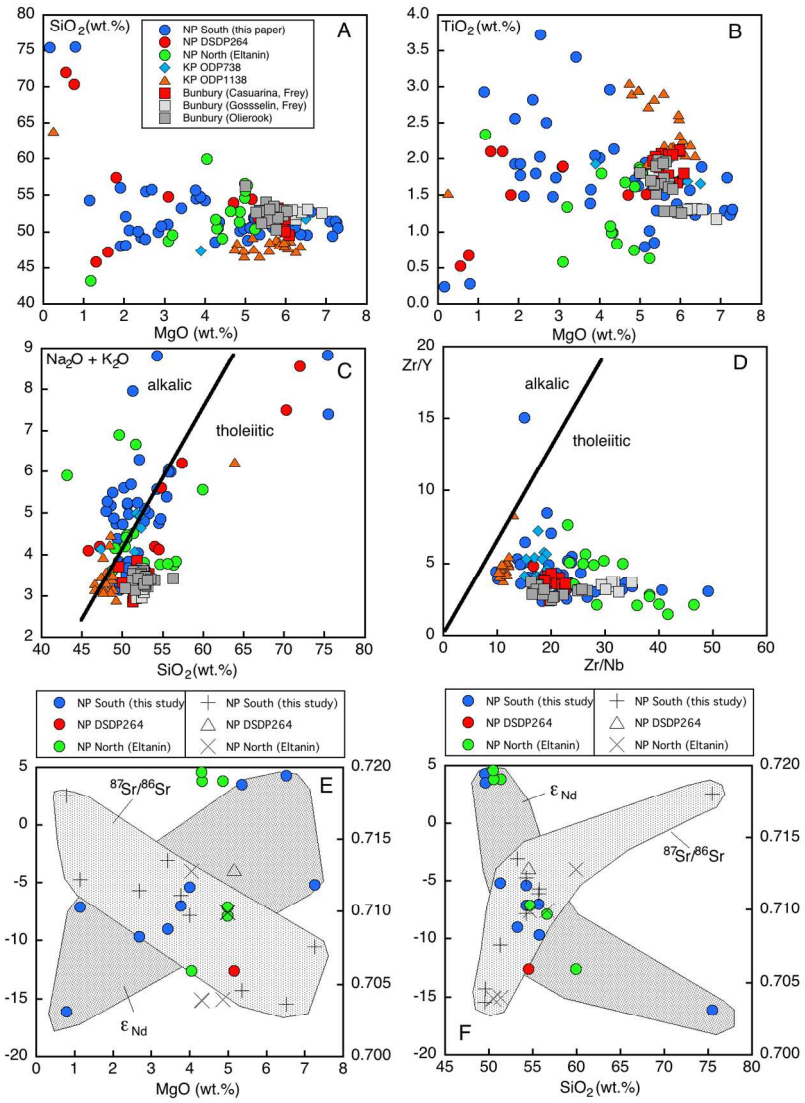

Figure 5 Major element compositions of Southern Surveyor 2005 cruise dredge samples from the southern margin of the Naturaliste Plateau. (A) SiO2 vs MgO. (B) TiO2 vs MgO. (C) Total Alkali Silica. TAS, diagram (after Le Bas et al., 1986), showing effects of submarine alteration scattering the alkali oxides. Panel D shows the Zr/Y vs Zr/Nb variations with the alkalic – subalkaline (tholeiitic) divide (after Pearce and Norry, 1979): this identifies almost all of the dredge samples as tholeiitic. (E, F) initial 87Sr/86Sr and εNd vs MgO and SiO2, respectively. Data for other sectors of the Naturaliste Plateau (DSDP site 264, Eltanin 1972 cruise, see Fig.1), for Cretaceous basaltic suites from the Kerguelen Plateau (KP, ODP sites 738 and 1138) and for ca.130 Ma Bunbury Basalt shown for comparison. Data sources: Ford, 1975; Coleman et al., 1982; Storey et al., 1992; Mahoney et al., 1995; Neal et al., 2002; Frey et al., 1996; Olierook et al, 2016).

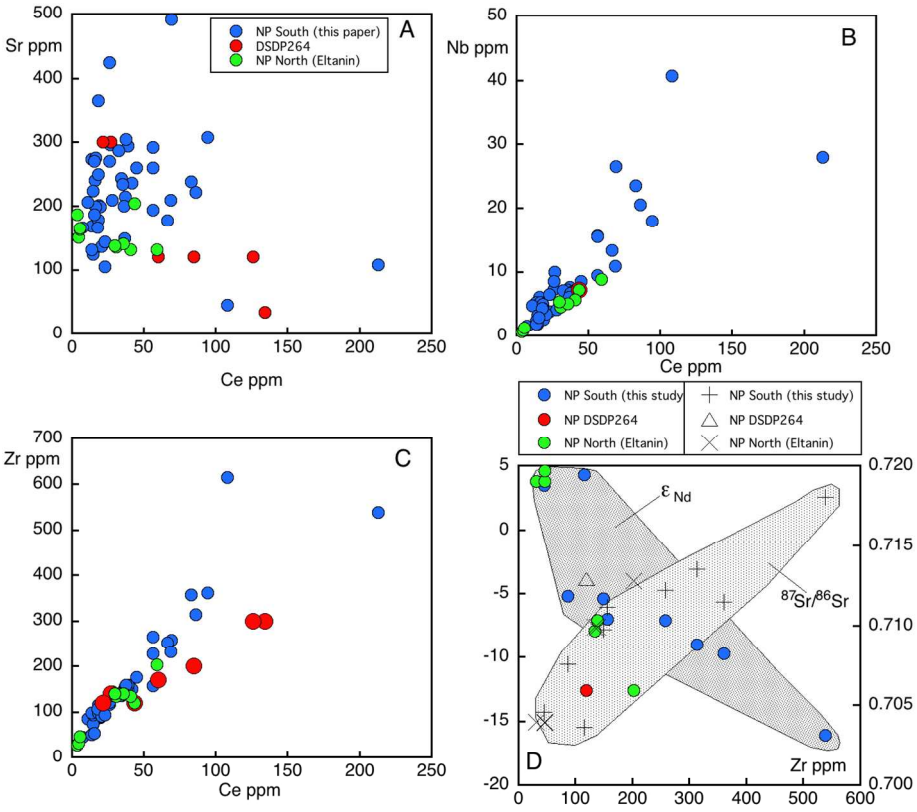

Figure 6 Trace element variations (A) Sr vs. Ce, (B) Nb vs. Ce; (C) Zr vs. Ce. Panel D shows covariation of initial 87Sr/86Sr and εNd with Zr concentration. This implies that the measured initial 87Sr/86Sr are robust, despite possible alteration effects on Sr concentrations (Fig.6a). Also shown are available data for DSDP Site 264 and from the Eltanin cruise, from the southern and northern Naturaliste Plateau, respectively. Data sources, see Fig.5.

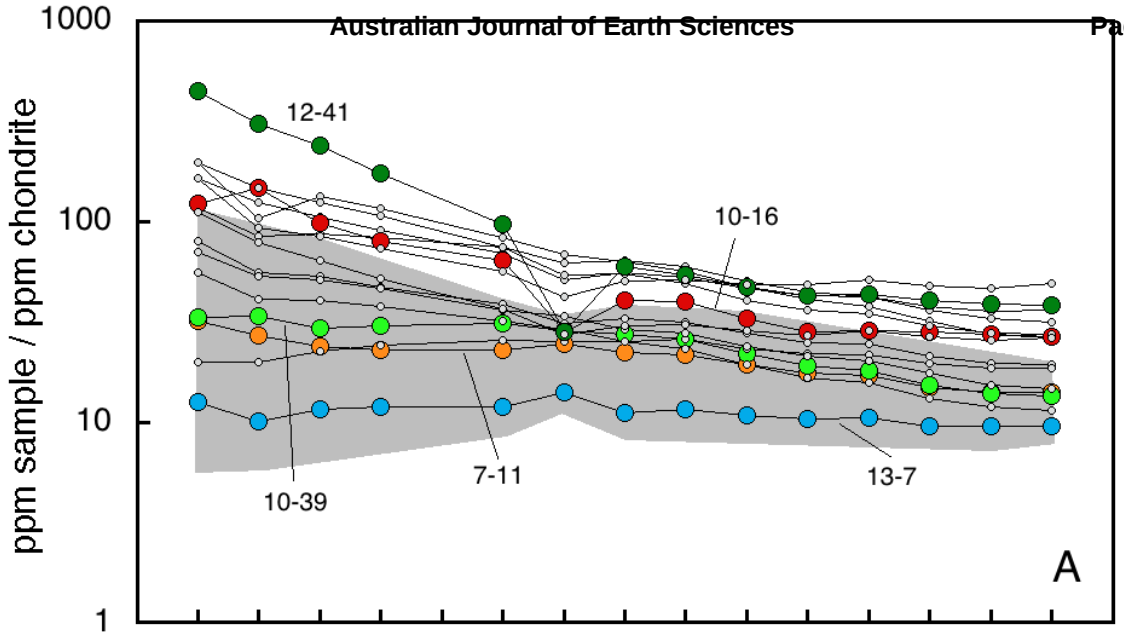

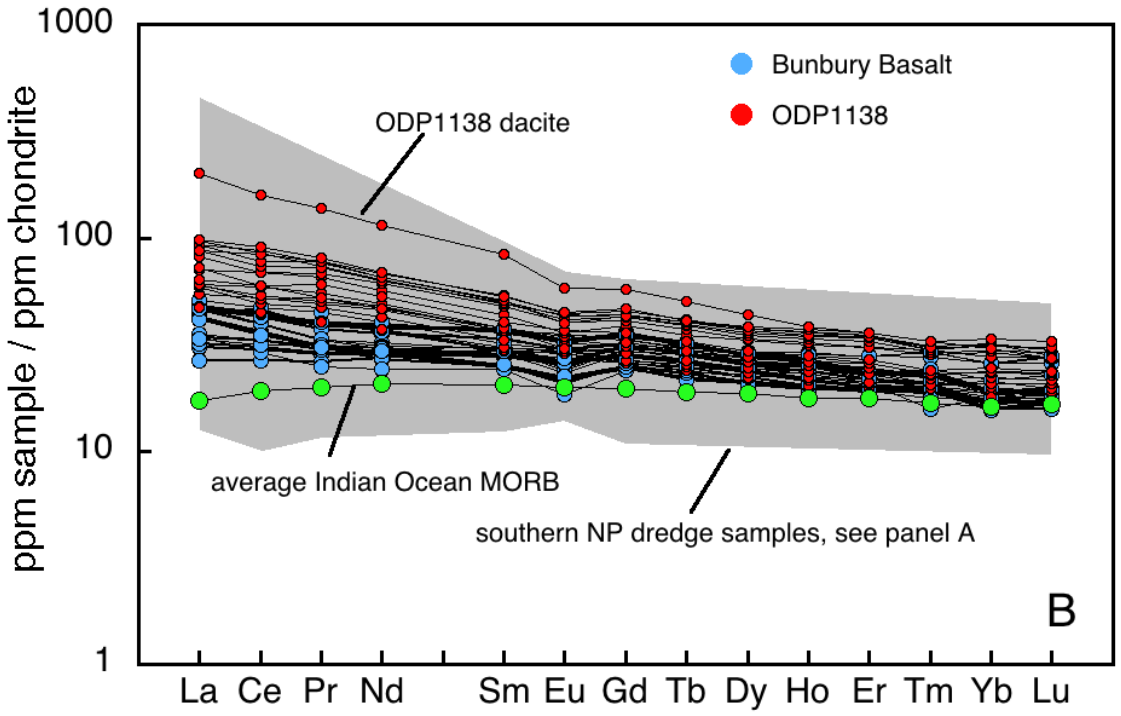

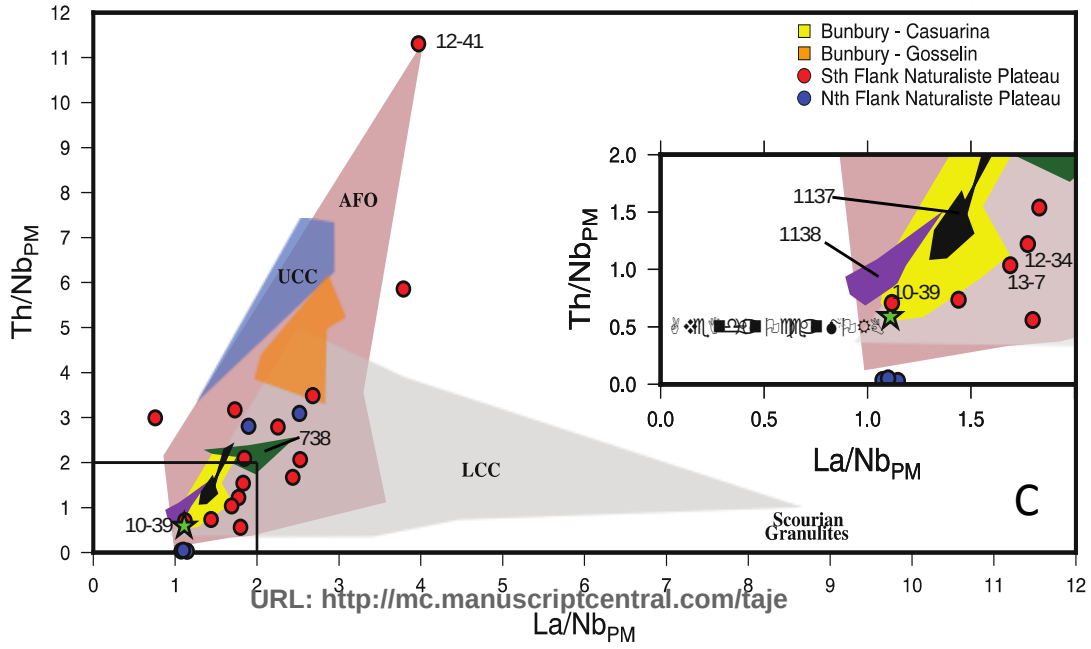

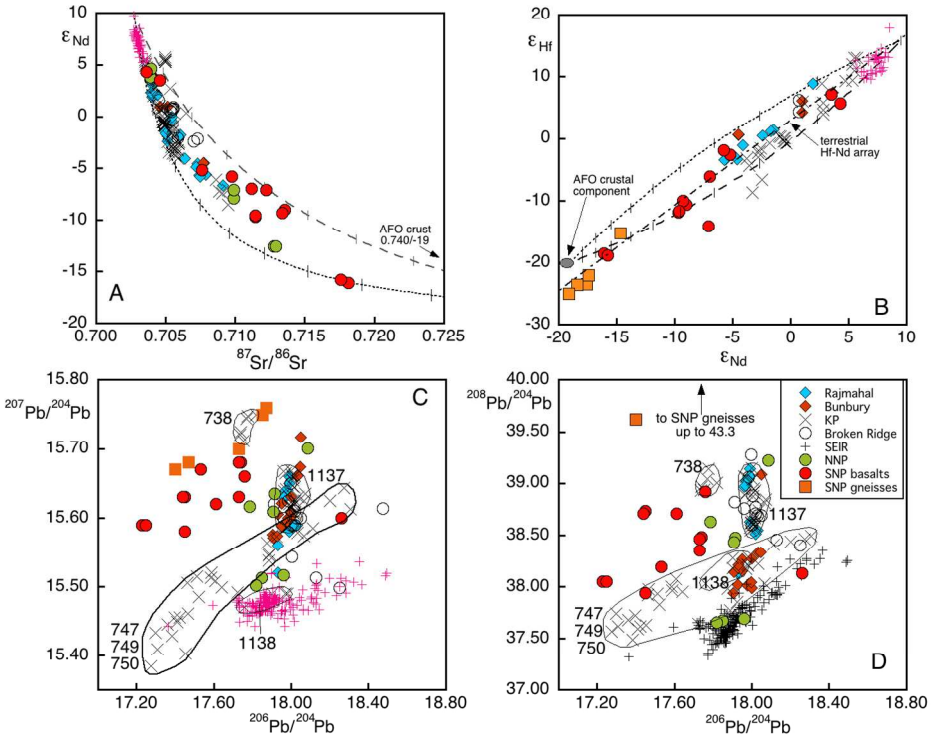

Figure 8: Sr-Nd-Pb-Hf isotope variations for Naturaliste Plateau dredge samples ('SNP basalts'), calculated at 130 Ma. Also shown are data for basalts from other sites on the northern Naturaliste Plateau ('NNP'), Bunbury Basalt, Rajmahal Traps, Broken Ridge, Cretaceous basalts from various ODP sites on the Kerguelen Plateau ('KP'), and modern MORB from the SE Indian Ridge ('SEIR'). (A) Sr-Nd isotopes, binary mixing lines drawn between a mantle endmember (300 ppm Sr, 87Sr/86Sr 0.7028, 10 ppm Nd, 143Nd/144Nd 0.51295, εNd +9.5) and two crustal endmembers modelled on data for the Albany Fraser Orogen (100 ppm Sr, 0.740, 40 ppm Nd, 0.51149, -19; 150 ppm Sr, 0.740, 20 ppm Nd, -19). (B) Hf-Nd isotopes, mixing lines are for two similar mantle endmembers (1-2 ppm Hf, 176Hf/177Hf 0.28315, εHf +15.8, 10 ppm Nd, 143Nd/144Nd 0.51295, εNd +9.5) and two similar crustal endmembers modelled on data for the Albany Fraser Orogen (4-5 ppm Hf, 176Hf/177Hf 0.282135, εHf -20.1, 30 ppm Nd, 143Nd/144Nd 0.51149, εNd -19.0). (C) 207Pb/204Pb vs 206Pb/204Pb. (D) 208Pb/204Pb vs 206Pb/204Pb. Data sources: Kent et al., 1997; Ingle et al., 2002, 2004; Storey et al., 1992; Frey et al., 1996, 2002; Ingle et al., 2002, 2003; Davies et al., 1989; Mahoney et al., 1995, 2002; Neal et al., 2002; Hanan et al., 2013; Mahoney et al., 2002; Graham et al., 2006) and dredged gneisses from the southern Naturaliste Plateau (orange squares, R.Maas unpubl.data).

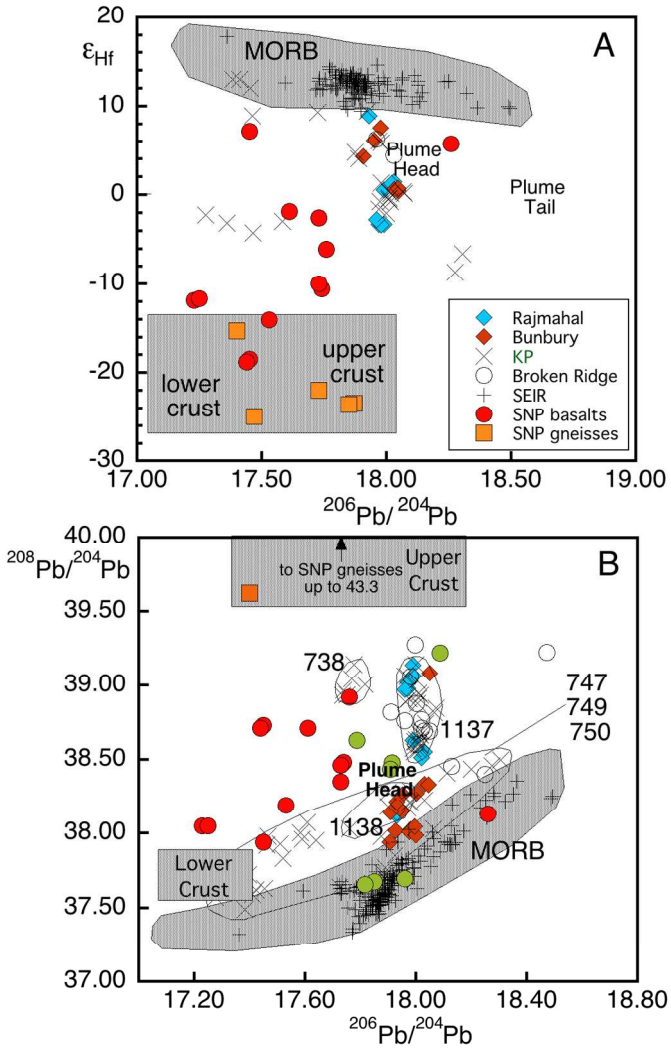

Figure 9 Hf-Pb and Pb-Pb isotope variations for Naturaliste Plateau dredge samples ('SNP basalts'), at 130 Ma. Also shown are data for basalts from other sites on the Naturaliste Plateau, Bunbury Basalt, Rajmahal Traps, Broken Ridge, Cretaceous basalts from various ODP sites on the Kerguelen Plateau, and modern MORB from the SE Indian Ridge (see Fig.8). Various inferred source components (Plume Head, Lower Crust, Upper Crust) inferred to be involved in the Cretaceous Kerguelen LIP and Naturaliste Plateau basalts (loosely modelled after Ingle et al., 2003) are shown for reference.

Table 1 SS09/05 Dredge location and contents

Station#	LOCALITY	START LAT	START LONG	END LAT	END LONG	DEPTH START	DEPTH END	TOTAL WEIGHT	DREDGE HAUL DESCRIPTION
DR3	Seamount at NW end of Leeuwin Escarpment	-34.7698	113.6449	-34.7664	113.6519	3851	3690	20kg	Cobbles of metaseds and volcanics plus several white muddy limestone cobbles
DR7	South facing scarp, south margin NP	-34.9021	112.9389	-34.8697	112.9424	3710	3200	100+kg	Altered vesicular mafic lavas, felsic lavas
DR10	South facing scarp, south margin NP	-35.0356	112.2374	-35.0358	112.2115	3752	3072	500kg	Coarse qtz-poor felsic intrusive (altered) + abundant altered mafic lavas, intrusives and lava breccia
DR11	South facing scarp, south margin NP	-35.1058	111.9827	-35.0969	111.9830	3600	3180	500kg	Angular blocks granodiorite, altered mafic lavas and lava breccia
DR12	South facing scarp, south margin NP	-35.0586	111.7235	-35.0393	111.7251	3700	3250	500kg	Altered mafic volcanics, felsic lavas
DR13	South facing scarp, south margin NP	-35.0349	111.6074	-35.0074	111.6140	3800	3130	500kg	Altered volcanics
DR16	South facing scarp, south margin NP	-35.0592	110.8759	-35.0577	110.8788	4140	3120	200kg	Weathered and altered mafic voclancis
DR20	South facing scarp, south margin NP	-35.0943	110.3241	-35.0908	110.3060	3850	3325	5kg	Altered mafic volcanics
DR21	South facing scarp, south margin NP	-35.0459	110.4159	-35.0410	110.4165	3900	3100	5kg in pipe dredge	Gneiss fragments

Table 2: Abundance of Major Elements (wt %)

Dredge #	Sample Description	SiO_2	TiO_2	Al_2O_3	Fe_2O_3	MnO	MgO	CaO	Na_2O	K_2O	P_2O_5	Loss inc S-	Total
3-2	Plagioclase-phyric, slightly vesicular basalt	54.28	2.93	18.56	8.71	0.08	1.14	4.81	3.47	5.33	0.67	2.67	99.66
3-3	Plagioclase-phyric dolerite	49.22	1.80	18.56	12.48	0.08	2.42	10.31	3.38	1.37	0.38	7.25	100.07
3-5	Altered glassy plagioclase-phyric basalt	52.12	1.77	19.66	12.20	0.08	2.03	5.55	3.30	2.99	0.29	6.78	99.74
3-7	Plagioclase-phyric basalt	50.18	1.49	20.76	13.17	0.06	2.13	6.43	3.26	2.33	0.18	6.28	99.74
7-2	Olivine-bearing dolerite	55.50	3.72	14.83	11.89	0.12	2.54	5.51	3.30	2.09	0.50	3.17	99.66
7-5	Olivine-bearing dolerite	53.23	3.41	13.27	14.02	0.17	3.42	7.05	2.99	2.00	0.45	2.38	100.46
7-10	Plagioclase-phyric basalt	51.41	1.29	17.45	9.62	0.11	7.10	9.14	3.40	0.34	0.12	3.63	99.75
7-11	Plagioclase-phyric basalt, relatively unaltered	51.27	1.27	17.00	10.10	0.14	7.26	9.33	3.18	0.31	0.13	2.55	99.85
7-28	Plagioclase-phyric basalt, moderate alteration	51.47	1.23	17.08	9.93	0.11	7.23	9.30	3.21	0.31	0.12	2.69	99.95
10-5	Plagioclase- and cliopyroxene-phyric basalt, slightly vesicular	50.01	2.82	15.40	16.52	0.25	2.35	7.08	3.77	0.97	0.84	4.85	100.14
10-14	Gabbro	49.96	1.48	21.76	8.71	0.14	2.85	10.53	3.37	0.86	0.34	2.23	99.94
10-16	Granophyre	75.39	0.24	12.39	2.81	0.03	0.16	0.12	3.86	4.98	0.03	0.82	100.11
10-39	Dolerite	49.54	1.89	15.13	13.12	0.28	6.52	9.42	3.20	0.64	0.26	2.77	99.70
10-67	Aphyric basalt	50.10	1.71	17.72	11.49	0.10	4.87	9.43	3.30	1.07	0.22	5.38	99.74
10-104	Very plagioclase phyric, vesicular basalt	54.52	1.58	19.35	8.70	0.13	3.79	6.90	3.45	1.31	0.29	6.10	100.05
11-8	Dolerite, quite altered	50.54	1.31	17.13	10.88	0.15	7.29	8.72	3.37	0.44	0.17	3.11	100.26
11-9	Coarsely plagioclase phyric basalt	55.75	2.50	14.49	12.97	0.12	2.68	4.87	3.16	2.90	0.56	2.08	100.15
11-19	Plagioclase+clinopyroxene (both fresh) and altered olivine-phyric basalt or microdolerite	52.10	1.56	15.51	11.32	0.16	5.28	10.34	3.09	0.49	0.15	1.20	99.92
11-20	Dolerite	51.92	1.94	14.74	12.56	0.17	5.21	9.20	3.44	0.60	0.22	1.50	100.24
11-25	Dolerite	49.37	1.74	16.81	11.87	0.15	7.16	8.23	3.62	0.77	0.27	2.96	100.00
12-1	Plagioclase phyric, slightly altered basalt	49.65	1.23	14.99	12.92	0.20	6.36	11.35	2.52	0.63	0.14	1.61	100.46
12-3	Plagioclase- and clinopyroxene-phyric dolerite, moderately altered	52.73	1.31	14.24	12.10	0.16	6.63	7.55	2.47	2.64	0.16	3.47	100.57
12-17	Plagioclase-phyric, altered basalt	51.37	2.13	16.31	14.21	0.15	4.36	7.41	2.84	0.91	0.30	4.62	99.81
12-18	Aphyric basalt	48.57	2.96	16.08	17.28	0.22	4.26	4.88	3.88	1.29	0.56	5.67	99.94
12-20	Aphyric altered basalt with fresh clinopyroxene	54.27	2.01	15.43	12.15	0.16	4.00	6.12	2.90	2.68	0.27	3.82	99.71
12-34	Massive Plagioclase- and Olivine-phyric basalt	50.62	1.61	14.85	12.93	0.19	5.68	10.78	2.82	0.36	0.16	1.15	99.95
12-38	Plagioclase-phyric basalt	48.95	2.03	18.16	15.97	0.22	2.52	6.55	2.96	1.91	0.73	5.65	99.71
12-41	Rhyolite, altered glass, quartz- K feldspar-phyric	75.47	0.28	12.10	2.90	0.05	0.79	0.90	3.36	4.04	0.11	1.90	99.68
12-53	Olivine- and Plagioclase-phyric, very altered basalt	54.76	2.04	15.36	13.84	0.14	3.88	4.81	2.98	1.88	0.32	5.18	99.92
13-1	Plagioclase-phyric, altered basalt	52.72	1.50	14.46	13.16	0.17	5.60	7.39	3.16	1.64	0.20	6.56	100.55
13-7	Plagioclase-phyric dolerite	49.61	0.85	21.10	7.71	0.09	5.35	11.87	2.88	0.43	0.09	2.89	100.41
13-34	Plagioclase- and Olivine-phyric basalt	51.28	1.70	16.89	12.36	0.17	6.00	3.45	4.21	3.74	0.20	7.11	99.96
13-36	Vesicular basalt with zeolites	48.81	1.81	18.24	13.02	0.09	5.06	7.20	3.72	1.77	0.27	4.81	99.67
13-47	Aphyric, slightly vesicular basalt	50.80	1.38	15.15	12.94	0.15	5.91	9.66	2.95	0.91	0.17	3.93	99.91
13-51	Clay altered Plagioclase-phyric basalt	51.05	1.89	17.42	13.31	0.16	3.08	6.90	3.19	2.50	0.50	5.76	100.29
13-52	Clay altered Plagioclase-phyric basalt	50.64	1.92	18.59	10.53	0.10	5.17	7.61	3.74	1.46	0.24	4.29	99.67
13-56	Plagioclase, clinopyroxene , altered olivine gabbro-dolerite	50.77	1.74	18.78	10.83	0.10	2.92	9.63	3.38	1.59	0.26	2.39	99.94
13-61	Large vesicular basalt	50.70	1.57	14.22	13.67	0.20	6.23	9.57	2.78	0.92	0.14	3.21	100.47
13-62	Plagioclase and altered olivine gabbro	50.61	1.95	18.83	10.09	0.09	5.13	7.80	3.71	1.53	0.25	3.94	99.94
16-2	Plagioclase-phyric vesicular basalt	55.99	1.93	14.48	14.47	0.16	1.90	4.59	2.90	3.10	0.50	3.97	99.90
16-9	Clinopyroxene- and Plagioclase-phyric gabbro	48.01	2.56	17.57	16.32	0.22	1.91	7.02	3.60	1.46	1.34	6.41	99.83
16-10	Clinopyroxene- and Plagioclase-phyric gabbro	50.53	0.79	18.27	10.70	0.16	5.12	9.90	2.79	1.62	0.11	3.72	99.75
20-1	Plagioclase- and cpx- phyric, segregation vesicles	55.66	1.39	13.29	12.79	0.16	3.77	6.74	3.53	2.46	0.22	2.54	99.99
20-8	Plagioclase-phyric, altered basalt	51.86	1.01	16.27	12.65	0.21	5.23	7.36	4.00	1.25	0.18	3.62	99.86
21-15	Moderately altered gabbro	48.13	1.93	17.11	19.11	0.24	2.03	5.83	2.79	2.49	0.33	5.63	99.73
21-17	Dolerite	51.74	1.29	14.54	13.75	0.16	5.41	9.42	2.77	0.75	0.16	2.12	99.51

Table 3: Abundance of Trace elements (ppm) Analyzed by X-Ray Fluorescence

Dredge	Rb	Sr	Ba	Sc	Cr	V	Ni	Cu	Zn	Zr	Nb	Y	Ce
3-2	89.9	491	1250	34.8	20.6	270	11.1	20	163	258	26.5	58.7	69.3
3-3	17.8	260	405	39.1	162	251	25.2	31.7	149	227	9.5	41.5	56.3
3-5	43.7	296	511	40.1	109	139	44.8	63.1	145	137	10	25.7	26.6
3-7	43.8	241	269	40.4	187	154	59.6	39.3	158	89.5	6.1	18	16
7-2	50.9	239	644	42.5	27	352	23.7	26.9	105	357	23.5	55.4	83.2
7-5	50.5	222	636	31.9	25.6	311	16	26.3	153	314	20.6	61.5	86.1
7-10	1.7	201	102	30.4	304	188	56.1	34.4	118	87.9	2.6	24.2	18.7
7-11	1.6	199	102	31.1	294	188	51.9	28.6	118	87.4	3.8	25.2	19.6
7-28	2.1	199	97.2	29.4	298	184	51.3	27.8	104	84.1	3.6	24.3	16.5
10-5	13	292	198	36.9	26.9	173	37.1	71.8	223	265	15.6	64.9	56.3
10-14	12.2	366	80	24.3	54.6	164	44.2	90.7	95.2	87.7	4.5	33.9	18.4
10-16	138	45.1	592	<2	2.7	19.2	5.6	11.9	81.4	614	40.7	40.8	108
10-39	10.4	270	113	32.6	144	245	79.8	87.6	125	116	7.3	28.6	26.2
10-67	22.9	274	36	37.8	350	224	68.4	112	325	85.5	5.2	24	13.7
10-104	54.9	275	58.5	36.9	306	194	77.1	129	254	85.7	5.2	24.3	16.4
11-8	8.5	270	141	29.2	234	196	84.3	44	159	82.1	3.8	20.8	15.6
11-9	75.5	307	961	29.5	11.5	234	26.2	26.7	174	361	18	51	94.4
11-19	12.7	207	196	39.8	205	274	51.2	110	106	84.4	4.7	28	11.1
11-20	27.3	250	70.1	37.8	318	286	46.5	71.6	111	115	4.9	31.4	18.4
11-25	15.9	424	247	27.8	81.6	189	77.9	33.6	131	121	8.5	24.5	26.4
12-1	19.2	124	79	49	255	345	105	143	98.8	73.3	3.2	28.7	14.6
12-3	104	224	306	41.2	174	259	77.7	107	127	93.4	1.9	30.3	14.7
12-8	29.9	105	129	53.6	96.1	402	72.4	168	118	126	3.8	39.6	22.8
12-17	20.3	215	103	42.3	206	247	70	96.5	155	156	7.6	37.4	37
12-18	23.9	178	123	42.1	64.2	357	107	125	275	252	13.4	59.8	66.6
12-20	71.5	236	329	39.6	198	248	72.4	85.1	154	150	7.3	35.4	42
12-34	8.7	169	32.3	49.3	195	348	61.6	135	114	97.3	2.4	30.8	14
12-38	39.5	210	152	55	159	296	120	264	252	144	4.1	42.3	28.2
12-41	125	108	809	2.2	1.9	20.3	32.2	26.1	103	539	28	63.7	213
12-53	50.8	200	310	38.5	174	202	89.5	110	203	149	6.7	35.5	36.1
13-1	15.3	179	102	44.2	99.7	279	45.3	135	113	98.2	4.3	30.9	18.3
13-7	12.1	167	51.3	42.8	228	252	66.9	94.9	90.4	45	1.6	15	7.49
13-34	58	244	533	23.1	61.1	152	70.9	53.5	115	135	5.3	31.1	34.6
13-36	96.1	294	347	25.6	59.6	192	77.9	55.2	148	147	7	33.9	39
13-47	20.8	137	64.3	57	82.5	361	55.1	141	141	90.9	3.4	33.7	20.6
13-51	73	234	236	38.4	103	168	75	110	184	142	7.2	39.8	35.4
13-52	25.8	294	374	24.7	65.9	175	68.5	49.3	127	159	6.9	30.7	39.1
13-56	28.6	287	360	35.6	113	261	42.3	44.3	54.3	139	7.1	28.4	32.6
13-61	14.5	167	100	46.8	112	341	43.2	93	110	106	4.3	31.6	18
13-62	26.3	304	386	26.7	65	182	65.5	50.9	108	159	6.7	31.3	37.6
16-2	68.8	260	310	46.4	35.6	368	48.2	121	181	175	8.5	42.8	44.8
16-9	21.2	210	261	64.6	35.6	509	67.4	160	268	232	10.9	81	68.7
16-10	57.4	132	122	47.6	134	272	83	131	144	50.7	1.9	19.2	14
20-1	71.5	194	463	36.6	33.5	330	30.8	67.2	98.4	157	15.5	40	56.4
20-8	37.1	187	233	51.3	154	294	93.7	153	118	53.1	2.9	22.3	15.5
21-15	52.2	149	248	70.7	121	562	106	107	242	138	6.1	40.6	36.8
21-17	20	144	228	51	71.2	387	44	80.1	116	93.9	6.5	26.2	23.2

Table 4: Abundance of Trace elements (ppm) Analyzed by ICP-MS

Dredge #	Li	Be	Rb	Sr	Ba	Sc	V	Cr	Co	Ni	Cu	Zn	Ga	Y	Zr	Hf	Nb	Ta	Pb	U	Th
3-2	10.1	1.26	85.6	478	1150	29.8	249	19.8	46.9	9.05	18.6	166	29	60.7	250	6.35	26.2	1.75	10.9	0.72	1.78
7-5	10.9	1.42	50.2	213	536	34.4	293	25.3	75.6	14.2	25.4	162	23.6	63.9	318	7.9	21.3	1.54	13	0.86	5.4
7-11	24.3	0.44	1.95	191	89.5	27.6	175	267	64.1	49.5	25.3	113	20.5	25.8	88.1	2.32	3.42	0.29	4.26	0.23	1.15
10-5	14.8	1.04	13.4	280	174	31.4	149	21.9	50.6	33.8	68.5	219	27.3	67.7	265	7.01	15.5	1.1	3.94	0.49	2.89
10-16	-	7.28	138	41.9	538	3.18	1.42	16.2	1.46	90.8	13	102	29	40.9	224	7.51	39.2	3.34	10.3	1.21	14.2
10-39	13.1	0.86	10.3	253	92.4	35.2	248	144	73.8	69.3	81	124	21.1	28.4	78.2	2.2	7.17	0.56	4.23	0.23	0.61
11-9	20.5	1.53	77.3	290	879	24	201	9.21	47.7	21.9	24.3	172	24.4	53.8	326	8.14	19.4	1.34	15.9	0.56	3.93
11-25	41.8	0.77	15.8	409	231	26.9	179	75.9	63.4	72	29.9	126	20.5	25	64.6	2.1	9.28	0.67	3.88	0.27	0.83
12-20	22.1	0.87	71.8	224	292	35.8	226	182	54.6	67.3	85.8	149	19.1	37.7	147	3.81	7.21	0.53	4.61	0.44	3.04
12-34	11.7	0.5	9.11	165	30.5	48.3	325	188	73.4	57.6	136	118	20.2	32.8	98	2.65	2.7	0.3	0.89	0.41	0.4
12-41	17.6	2.86	129	103	793	3.46	17.7	1.14	42.7	30.5	27.4	105	14.9	66.1	404	11.5	27	1.98	30.3	2.21	36.9
13-7	38.1	0.27	12.1	158	41.2	37.5	222	220	70.4	63.2	88.7	95.2	18.1	15.2	43.4	1.21	1.79	0.17	0.46	0.15	0.22
13-52	54.1	0.8	26.5	281	329	26.1	171	65.5	54.3	65.1	48.6	133	22.4	32	157	3.96	6.68	0.49	4.88	0.29	1.67
16-9	30.9	1.24	22.1	199	226	54.7	434	31.1	74.5	63.6	162	269	27.2	85.2	229	6.11	10.4	0.69	12.2	2.07	7.36
20-1	11.9	0.77	71.1	182	427	38.3	298	29.5	62.4	28.4	65	100	18.6	41.3	153	4.01	15.5	0.82	7.14	0.69	5.95

Table 5: Radiogenic isotopes: Rb-Sr, Sm-Nd, Lu-Hf, and U-Th-Pb

sample	3-2 basalt	7-5 dolerite	7-11 basalt	10-39 dolerite	11-9 basalt	12-20 dolerite	12-41 rhyolite	13-7 dolerite	20-1 basalt
Rb ppm	85.6	50.2	1.99	10.34	77.3	71.9	129.2	12.12	71.1
Sr ppm	478.4	213.0	191.2	253.4	290.0	224.1	102.6	158.5	181.7
$^{87}Rb/^{86}Sr$	0.518	0.683	0.030	0.118	0.772	0.928	3.650	0.221	1.132
$^{87}Sr/^{86}Sr$	0.713171	0.714781	0.707639	0.70383	0.712857	0.711437	0.724667	0.704974	0.713197
Sm ppm	12.72	10.66	3.51	4.74	11.38	5.93	14.84	1.83	5.64
Nd ppm	54.34	42.35	10.75	14.11	49.57	22.11	80.81	5.57	24.14
$^{147}Sm/^{144}Nd$	0.142	0.152	0.198	0.203	0.139	0.162	0.111	0.199	0.141
$^{143}Nd/^{144}Nd$	0.512221	0.512134	0.512369	0.512858	0.512087	0.512309	0.511736	0.512816	0.512226
ε_{Nd} now	-8.0	-9.7	-5.1	4.4	-10.6	-6.3	-17.5	3.6	-7.9
Lu ppm	0.67	0.92	0.36	0.34	0.69	0.49	0.97	0.24	0.67
Hf ppm	6.35	7.9	2.32	2.2	8.14	3.81	11.46	1.21	4.01
$^{176}Lu/^{177}Hf$	0.0150	0.0165	0.0220	0.0219	0.0120	0.0183	0.0120	0.0282	0.0237
$^{177}Hf/^{177}Hf$	0.282341	0.282444	0.282683	0.282919	0.282396	0.282694	0.282211	0.282974	0.282588
ε_{Hf} now	-15.7	-12.1	-3.6	4.7	-13.8	-3.2	-20.3	6.7	-7.0
U ppm	0.72	0.86	0.23	0.23	0.56	0.44	2.21	0.15	0.69
Th ppm	1.78	5.4	1.15	0.61	3.93	3.04	36.92	0.22	5.95
Pb ppm	10.91	13.03	4.26	4.23	15.9	4.61	30.31	0.45	7.14
$^{238}U/^{204}Pb$	4.1	4.2	3.4	3.4	2.2	6.0	4.6	20.9	6.2
$^{232}Th/^{204}Pb$	10.6	27.1	17.6	9.4	15.9	43.2	79.9	31.7	54.9
$^{206}Pb/^{204}Pb$	17.618	17.822	17.793	18.327	17.277	17.727	17.539	17.867	17.885
$^{207}Pb/^{204}Pb$	15.671	15.684	15.637	15.602	15.592	15.622	15.632	15.597	15.664
$^{208}Pb/^{204}Pb$	38.253	38.654	38.464	38.186	38.150	38.989	39.241	38.146	39.267
age-corrected isotope ratios (130 Ma)									
$^{87}Sr/^{86}Sr_i$	0.71223	0.71354	0.70758	0.70362	0.71146	0.70975	0.71804	0.70457	0.71114
$^{143}Nd/^{144}Nd_i$	0.512100	0.512005	0.512201	0.512685	0.511969	0.512171	0.511642	0.512647	0.512106
ε_{Ndi}	-7.1	-9.0	-5.2	4.3	-9.7	-5.7	-16.1	3.5	-7.0
$^{176}Hf/^{177}Hf_i$	0.282305	0.282404	0.282630	0.282866	0.282367	0.282650	0.282182	0.282906	0.282530
ε_{Hfi}	-14.1	-10.6	-2.6	5.8	-11.9	-1.9	-18.4	7.2	-6.1
$^{206}Pb/^{204}Pb_i$	17.53	17.74	17.72	18.26	17.23	17.60	17.45	17.44	17.76
$^{207}Pb/^{204}Pb_i$	15.67	15.68	15.63	15.59	15.59	15.62	15.63	15.58	15.66
$^{208}Pb/^{204}Pb_i$	38.18	38.48	38.35	38.13	38.05	38.71	38.73	37.94	38.91

Sr-Nd-Hf isotopes determined on powders made in a tungsten carbide mill, Pb isotopes on handpicked chips; trace element concentrations and parent/daughter ratios for powders made in an agate mill and measured by ICP-MS. Powders and chips used for isotope work were leached in hot 6M hydrochloric acid for 1 hour and rinsed with distilled water, followed by dissolution on a hotplate (3:1 HF-HNO_3, 2 days, 100°C; 6M HCl, 1 day, 100°C). Sr and Nd were extracted on EICHROM Sr-, TRU- and LN-resin (Pin et al., 1994; Pin and Zantos-Saldegui, 2000); Hf was extracted on EICHROM LN-resin using the technique of Münker et al. (2001). Pb was extracted on 0.1 ml columns of AG1-X8 (100-200) anion exchange resin (Manhes et al). Isotope ratios determined on a NU Plasma MC-ICPMS coupled to an ARIDUS desolvating device, with typical signals of 6-8V Sr, 10-20V Nd-Hf and 8-12V Pb (Woodhead, 2002; Maas et al., 2005; Kamenetsky et al., 2009). Instrumental mass bias for Sr, Nd and Hf corrected by internal normalization to $^{88}Sr/^{86}Sr$=8.37521, $^{146}Nd/^{145}Nd$=2.0719425 (equivalent to $^{146}Nd/^{144}Nd$ = 0.7219) and 179Hf/177Hf=0.7325, respectively, and data are reported relative to SRM987 = 0.710230, La Jolla=0.511860 and JMC475 = 0.282160. Internal precision (2se) is ±0.000020 (Sr), ≤±0.000014 (Nd), ±0.000008 (Hf); external precision (2sd) is ±0.000040 (Sr); ±0.000020 (Nd), ±0.000015 (Hf). ε_{Nd} and ε_{Hf} values calculated for Bulk Earth compositions of $^{147}Sm/^{144}Nd$ =0.1967, $^{143}Nd/^{144}Nd$=0.512638, $^{176}Lu/^{177}Hf$=0.0332, $^{176}Hf/^{177}Hf$=0.282772. Mass bias in Pb isotope runs corrected using the thallium doping technique of Woodhead (2002); for total Pb signals near 10V, this produces external precisions of ±0.04-0.09% (2sd). Results (±2sd external) for various isotopic and rock standards over the period 2009-2010: modern seawater, EN1 0.709163±31 (n=25), E&A 0.708010±42 (n=7), BCR-2 0.705004±39 (n=10), 0.512644±24 (n=11), 0.282878±13 (n=9), BHVO-2 0.703456±37 (n=4), 0.512985±16 (n=7), 0.83113±17 (n=9), JNd-1 0.512115±11 (n=12). Pb isotope results for BCR-2 over the period 2010-2011 (n=22) 18.759±0.039%, 15.621±0.064%, 38.730±0.087%. All results are consistent with TIMS reference values.

Age corrections were done with parent/daughter ratios based on ICP-MS trace element data for separate powders from the same samples, with the possibility of bias due to sample heterogeneity. Age corrections for Nd and Hf isotopes are very small and any additional error from age corrections would be smaller than external precisions on measured $^{143}Nd/^{144}Nd$ and $^{176}Hf/^{177}Hf$. Age corrected $^{87}Sr/^{86}Sr$ carry uncertainties (from Monte Carlo modelling) of ±0.00004 – 0.00012 (2sd) for the Rb/Sr range observed in the basalts (see above, Rb/Sr ±5%, age ±2Ma). Rhyolite DR12 (sample 12-41) has a higher Rb/Sr ($^{87}Rb/^{86}Sr$ 3.65) and a propagated uncertainty in $^{87}Sr/^{86}Sr_{128}$ of ±0.00039. Propagated uncertainties in initial Pb isotope ratios are ±0.01 (0.03), <±0.01, ±0.03 (0.04), respectively (U/Pb, Th/Pb ratios assumed to have precisions of %5, numbers in brackets are for samples with highest U/Pb and Th/Pb, respectively.

Decay constants: ^{87}Rb 1.42 10^{-11}/y; ^{147}Sm 6.54 10^{-12}/y; ^{176}Lu 1.865 10^{-11}/y; ^{238}U 0.155125 10^{-9}/y, ^{235}U 0.98485 10^{-9}/y, ^{232}Th 0.049475 10^{-9}/y

Supplementary Material Appendix 1: Selected Rock Sample Photos, *RV Southern Surveyor* Voyage 2005/09. Scale is an Australian 20 cent piece.

DR10–11

DR10–107

DR11–14

DR 11-7

DR12–9

DR12–19

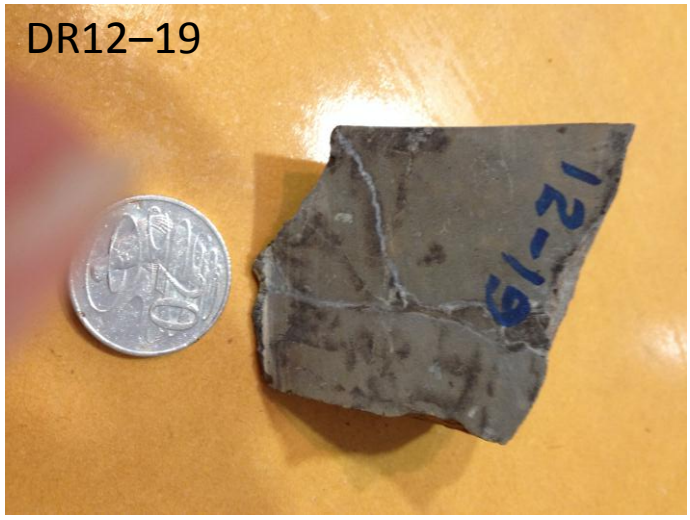


DR13–8
13-8


DR13–17
13-17


DR13–22
13-22


DR13–58
13-58

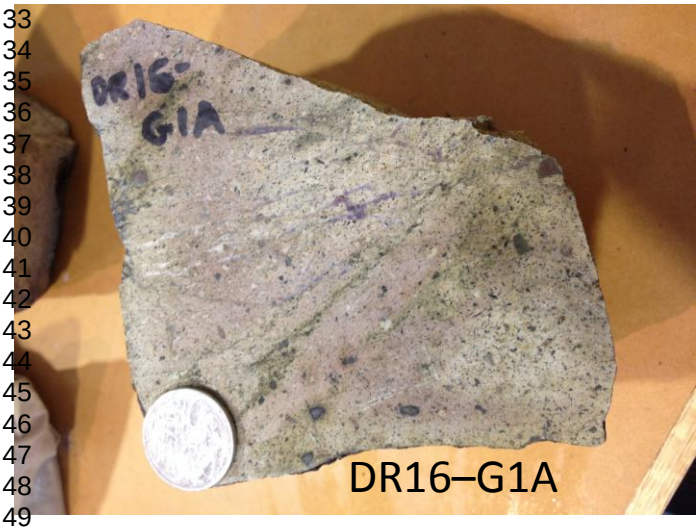
DR16-
G1A
DR16–G1A

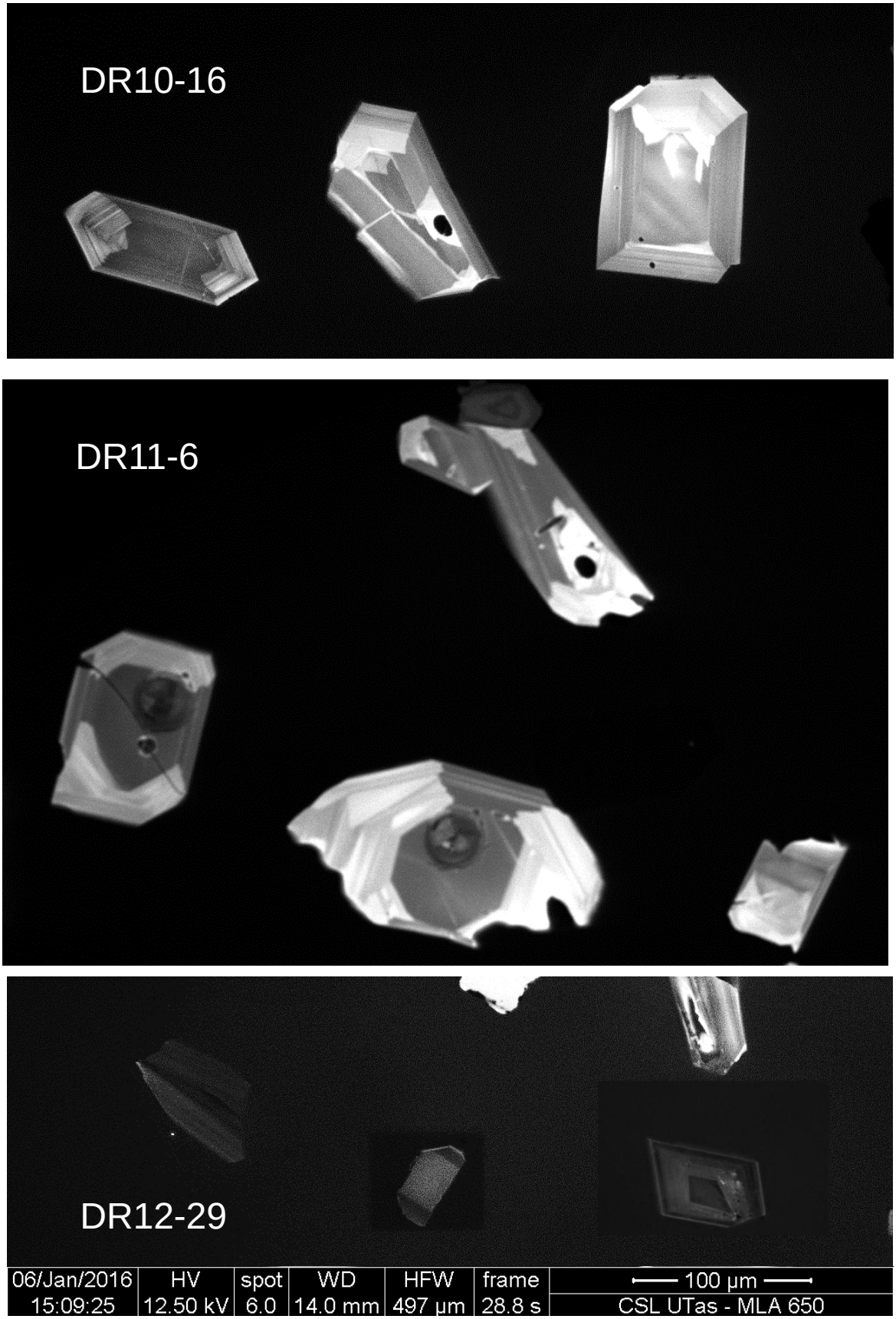

Cathodoluminescence images of zircons from the samples analysed in this study

Supplementary Material Appendix 2 X-ray fluorescence (XRF) major and trace element analysis methods, and laser ablation inductively coupled plasma mass spectrometry (LA_ICPMS) U/Pb zircon geochronology methods

XRF: Samples were powdered in a tungsten carbide mill. Concentrations of major elements and selected trace elements were determined using a Phillips PW1480 X-ray spectrometer at the University of Tasmania with LiF200, LiF220, PX-1, PE002 and Ge111 crystals. Major elements were determined on fusion discs prepared at 1100˚C in a 5% Au-95% Pt crucible, with trace elements determined on a pressed powder (10 g) pellet. Corrections for mass absorption were calculated using Phillips X40 software with De Jongh's calibration model and Phillips alpha coefficients. Calibration was achieved using pure element mixes in pure silica, along with international and Tasmania University standard rocks. See Yu et al. (2001) for further details.

LA-ICPMS: ICP-MS trace element analyses at UTAS were obtained using the methods of Robinson et al. (1999) and Yu et al. (2000). The analyses were done on duplicate high-pressure HF-HClO4 digestions. Sub-boiling double distilled acids and ultrapure water were used, to clean sampler and skimmer cones, ICP torch, spray chamber, nebulizer and sample introduction tubes (including auto-sampler tubing). Prior to sample analysis the instrument was purged for at least 24 hours with 5% v/v HNO_3 and 0.05% v/v HF rinse solution.

Several elements, Ce, Ba, Sr, Rb, Zr, Cr, and Y were analyzed by both XRF and ICP-MS. Plots of element abundance determined by XRF vs. ICP-MS for correlation coefficients are x,y,z etc. for these elements. Of course, such agreement is not found for every element; e.g. neither La nor Th are determined precisely or accurately by XRF.

The zircons from the igneous rocks from the Naturaliste Plateau were separated at the University of Tasmania. 200 g of rock was crushed for 10 seconds in a Cr-steel ring mill producing medium to coarse sand. Non-magnetic heavy minerals were then separated from the crushed material using a gold pan and a Fe-B-Nd hand magnet. The zircons were hand picked from the non-magnetic heavy mineral concentrate under the microscope in cross-polarised transmitted light. The selected crystals were placed on double-sided sticky tape and epoxy glue was then poured into a 2.5 cm diameter mould on top of the zircons. The mount was dried for 12 hours and polished using clean sandpaper and a clean polishing lap. Samples were then washed in distilled water in an ultrasonic bath prior to analysis

The analyses in this study were performed on an Agilent 7500cs quadrupole ICPMS with a 213 nm New Wave solid state laser fitted with a custom made, low volume ablation cell at the University of Tasmania in Hobart. The down hole fractionation, instrument drift and mass bias corrections for Pb/U ratios were calculated using 2 analyses on the primary standard zircons (Temora: Black et al., 2003) analysed at the beginning and end of the session and every 12 unknown zircons (roughly every 1/2 hour) using the same spot size and conditions as used on the samples. The spacing of the primary standards in the analytical sequence was optimised to provide the most accurate drift correction curve on the instrument. Using fewer standards analysed more frequently can lead to problems with over-fitting of the drift

correction curves and increases scatter of the ages on the samples. Secondary standards were also analysed between each batch of samples (91500, Mud Tank, 98-521 zircons: Black et al., 2003; Black & Gulson, 1978; Harris et al., 2004) The mass bias and drift for the $^{207}Pb/^{206}Pb$ ratio was corrected using large spots on NIST610 which was analysed after every 36 unknown zircons.

Each analysis began with a 30 second blank gas measurement followed by a further 30 seconds of analysis time when the laser was switched on. Zircons were sampled on 32 μm spots using the laser at 5 Hz and a density of approximately 12 Jcm^{-2}. A flow of He gas carried particles ablated by the laser out of the chamber to be mixed with Ar gas and carried to the plasma torch. Isotopes measured were ^{96}Zr, ^{146}Nd, ^{178}Hf, ^{202}Hg, ^{204}Pb, ^{206}Pb, ^{207}Pb, ^{208}Pb, ^{232}Th and ^{238}U with each element being measured every 0.19 s with longer counting time on the Pb isotopes (30 ms) compared to the other elements (10 ms). ^{235}U was calculated from ^{238}U assuming $^{238}U/^{235}U = 137.88$. The data reduction method used was similar to that reported in Sack et al. (2011), and propagation of uncertainties was similar to that described by Paton et al. (2010). Integration intervals were chosen using a method similar to that described by Petrus and Kamber (2012), where the time-resolved signal from each analysis is examined on the concordia diagram to identify and remove zones with Pb-rich inclusions or Pb loss.

Element abundances on zircons were calculated using Zr as the internal standard element, assuming stoichiometric proportions and using the 91500 standard correct for mass bias and drift.

The data collected is shown in Table A2-1 and Figure A2-1.The individual zircon data is plotted and tabled at 1 sigma to make the diagrams less cluttered and easier to read, but uncertainties on the ages calculated by Isoplot (Ludwig, 2009) are quoted at 2 sigma. The Tera-Wasserburg diagrams shown in the figures make it easier visualise the trends towards common Pb and the intersection of this trend with Concordia. The Wetherill-type Concordia have also been plotted in the data appendix (Excel) for convenience. Also included in the spreadsheets are the raw count rates, and data from the various standards that were analysed in the same analytical run as the samples.

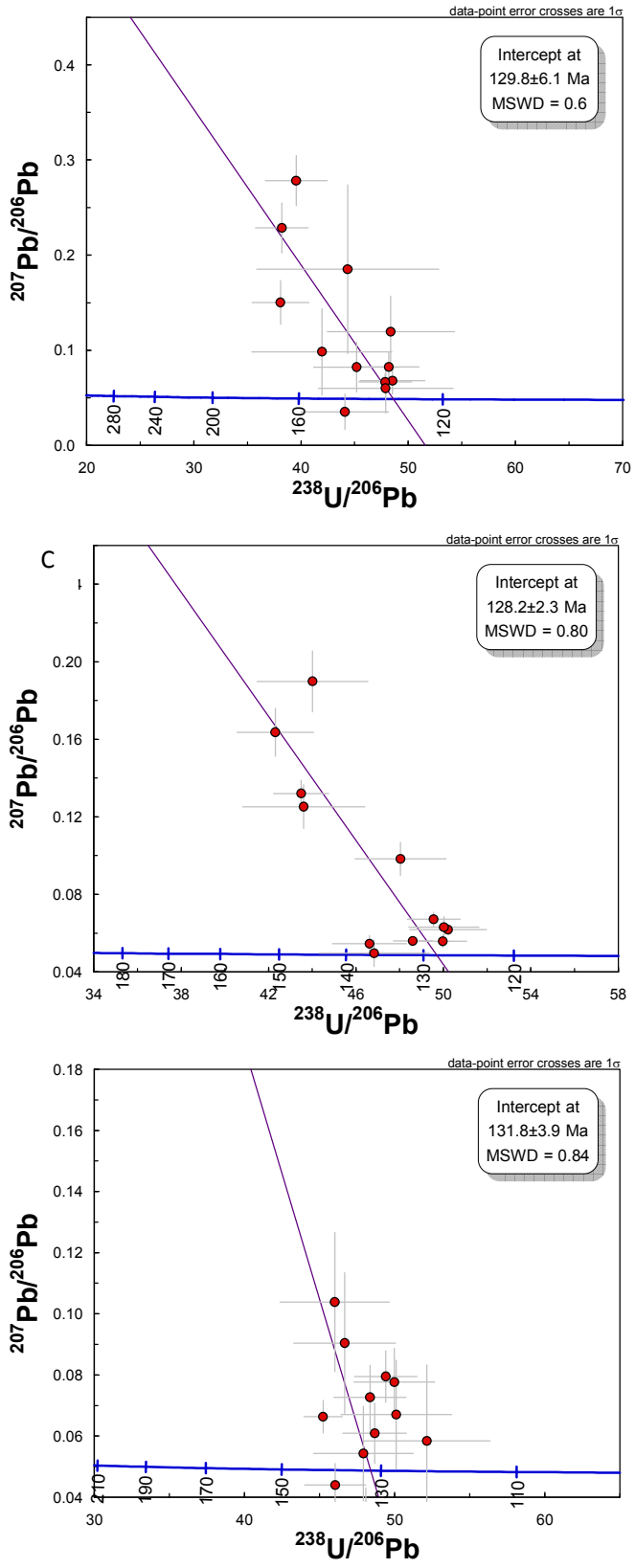

Figure1a,b and c Tera-Wasseburg plot of LA-ICPMS U-Pb isotopic zircon data from the zircons recovered from the cruise. Regressions are towards common Pb at 128 Ma.

Supplementary Material Appendix 3: $^{40}Ar/^{39}Ar$ methods and analytical results

The samples for $^{40}Ar/^{39}Ar$ geochronology were selected based on the appearance of plagioclase phenocrysts or microphenocrysts within rocks that were least affected by seafloor alteration. The freshness of plagioclase was examined by thin section petrography. Sample DR11-19 contains plagioclase phenocrysts up to 5 mm long in a grey groundmass; DR12-8 has plagioclase laths <1 mm long set in a mid-brown groundmass; and DR13-33 has plagioclase phenocrysts up to 15 mm long set in a light-brown groundmass.

The samples were crushed and sieved to the dimensions listed in the table below, and washed in tap water in an ultrasonic bath to remove adhering dust. Plagioclase was separated by firstly using a Franz Isodynamic Separator to remove the magnetic fraction, followed by heavy-liquid separation using LST fluid, with density controlled by the addition of distilled water. To remove clays and other adhering alteration phases, the resultant separate was then cleaned in an ultrasonic bath using sequential washes of tap water, distilled water, and distilled water plus ethanol. Each wash lasted approximately 1 hour. The separates were then air-dried, and plagioclase crystals handpicked with the aid of a binocular microscope and fine tweezers. Optically clear crystals were selected, avoiding areas of iron staining, cloudiness, or inclusions of other minerals, melt, or fluid.

The plagioclase separates were wrapped in Al-foil, and placed in 7-pit Al disks, with grains of Fish Canyon sanidine (28.294 ± 0.072 Ma, 2σ, Renne et al. 2011) and GA1550 biotite (99.738 + 0.208 Ma, 2σ, Renne et al. 2011) loaded into separate pits. The irradiation disks were closed with aluminium covers, wrapped in aluminium foil, and vacuum heat-sealed into quartz vials. These quartz vials were irradiated for 14 hours at the B-1 Cadmium-lined in-core irradiation tube facility at the Radiation Center, Oregon State University, USA. Before analysis, the mineral grains and fluence monitors were baked-out under vacuum at ~200°C for ~12 hours. J-factors were calculated using laser total-fusion analyses of 15 single Fish Canyon sanidine crystals from each disk. Four aliquots of GA1550 biotite were also analysed via the laser heating device, and the results provide an important cross-check on the J factors.

Sample	Lab #	Weight plagioclase analysed (mg)	Weight aluminium foil (mg)	Grain size (μm)	Decay (months)
DR11-19	4565-01	86	30	106-425	10
DR12-8	4570-01	90	30	106-425	10
DR13-33	4558-01	74	34	355-1000	5

After a decay period spanning 5 months (for sample DR13-33) or 10 months (for samples DR11-19 and DR12-8), the samples were incrementally heated in a double-vacuum resistance furnace fitted with an Omega temperature controller. For each heating step, the samples (and Al-foil wrapping) were held at the required temperature for a minimum of six minutes. The gas released in each step was cleaned through a cryocooled cold-trap (T = -137°C) and two C-50 SAES Zr-V-Fe getters (one hot, the other at room temperature of 20°C) and analysed for Ar isotopes in a MAP-215-50 mass spectrometer equipped with a third C-50 SAES Zr-V-Fe getter (at room temperature).

Room-temperature blanks, hot blanks (500°C), and room-temperature air pipettes were analysed before and after each sample. For all analyses (blanks, airs, and unknowns) first-stage cleanup (gas exposed to the hot getter and cold finger) extended for 2100 seconds (35 minutes), and second stage cleanup (gas also exposed to the room-temperature getter) extended for 420 seconds (7 minutes). The gas was then inlet to the mass spectrometer, where data was collected

in peak-hopping mode, with eight cycles of data collection at masses 40, 39, 38, 37, 36, and multiplier baseline.

Data was corrected for blanks, mass discrimination, nucleogenic interferences, and atmospheric contamination and used to calculate apparent ages for each degassing step. For data regression we used the software "MassSpec Version 8.131" developed by Alan Deino of the Berkeley Geochronology Centre, USA. Air pipette analyses yielded a discrimination value of 1.00217 ± 0.00408 (2σ, n = 40), using the Power Law and the $^{40}Ar/^{36}Ar$ value of 298.56 ± 0.31 for atmospheric argon (Lee et al. 2006, Renne et al. 2009). Laboratory automation and analytical procedures are described in Deino and Potts (1990) and Vasconcelos et al. (2002). All ages are reported using the potassium decay constants of Steiger and Jäger (1977). All decay constants and irradiation parameters used are reported in the Supplementary Excel table.

Naturaliste $^{40}Ar/^{39}Ar$ results

In this study we define an age plateau as a sequence of three or more contiguous steps corresponding to at least 50% of the total ^{39}Ar released, and whose age values overlap within 2σ uncertainty (Fleck et al. 1977, McDougall and Harrison 1999). Plateau ages were calculated as the mean weighted by inverse variance. Plateau age uncertainties were calculated as the standard error of the weighted mean, but if the MSWD was greater than 1, then the uncertainties were calculated as the standard error of the weighted mean multiplied by the square root of the MSWD. The plateau age uncertainties are 2σ and include the uncertainty in J, but do not include the uncertainty in the potassium decay constants.

Isochrons are plotted for plateau steps only; magenta-coloured ellipses represent the non-plateau steps that were eliminated from the isochron age calculation. The light-brown dashed lines on isochrons indicate the 2σ uncertainty envelopes. Isochron ages were calculated from the $^{39}Ar/^{40}Ar$ intercept, and isochron age uncertainties were calculated using a York regression (York 1969). Isochron age uncertainties are reported at the 95% confidence level (2σ), and include the uncertainty in the irradiation correction factors and the uncertainty in J, but do not include the uncertainty in the potassium decay constants.

Analyses from DR11-19 and DR12-8 yield precise results, reflecting their relatively high K/Ca and $\%^{40}Ar^*$ values. Analyses from DR13-33 are less precise, reflecting the lower K/Ca and $\%^{40}Ar^*$ yields. For both DR11-19 and DR12-8 the $\%^{40}Ar^*$ values decrease at the higher-temperature end of the heating schedule, reflecting an increased atmospheric argon contribution from heating of the resistance furnace itself.

Plateaus comprise 64 to 82% of the ^{39}Ar released, indicating that these results are reliable determinations for the age of eruption. Low-temperature steps yield younger ages characteristic of some argon loss, likely via incipient seawater alteration of the plagioclase. The reliability of the ages is supported by the concordance between the $^{40}Ar/^{39}Ar$ isochron and $^{40}Ar/^{39}Ar$ plateau ages, the excellent agreement between GA1550 analyses 99.8 ± 0.8 Ma (2σ, n = 31) and the accepted age for this material (99.738 + 0.208 Ma, 2σ, Renne et al. 2011), as well as the concordance between the $^{40}Ar/^{39}Ar$ and zircon U-Pb ages. Initial $^{40}Ar/^{36}Ar$ values on isochron diagrams are within analytical uncertainty of modern-day atmosphere, indicating these samples are free from inherited argon.